Thermomechanical Analyses of Metal Solidification Processes

by

Winnie C. M. Leung

Submitted to the Department of Mechanical Engineering
in Partial Fulfillment of the Requirements for the Degree of

Master of Science in Mechanical Engineering

at the

MASSACHUSETTS INSTITUTE OF TECHNOLOGY

February 1995.

Signature of Author _____
Department of Mechanical Engineering

Certified by: _____
Dr. Peter J. Raboin
Company Supervisor, Lawrence Livermore National Laboratory

Certified by: _____
Professor Merton C. Flemings
Thesis Supervisor, Department of Materials Science and Engineering

Certified by: _____
Professor Carl R. Peterson
Departmental Reader, Department of Mechanical Engineering

Accepted by: _____
Professor Ain A. Sonin
Graduate Thesis Committee

Thermomechanical Analyses of Metal Solidification Processes

by

Winnie C. M. Leung

Submitted to the Department of Mechanical Engineering on January 20, 1995 in partial fulfillment of the requirements for the degree of Master of Science in Mechanical Engineering.

Abstract

Coupled thermal and mechanical finite element analyses were used to model the solidification of metal castings. A constitutive material model capable of predicting the flow strength of mushy metals was developed using rate dependent plasticity. A model addressing the reduction in heat transfer across casting-mold interfaces was created. Thermomechanical analyses of a simple casting experiment generated realistic predictions which showed some discrepancies with experimental results. Analysis of a hot tear experiment was successful in providing explanations to why past experiments had failed.

Company Supervisor: Dr. Peter J. Raboin

Thesis Supervisor: Dr. Merton C. Flemings
Department Head of Material Sciences and Engineering

Departmental Reader: Dr. Carl R. Peterson
Associate Professor of Mechanical Engineering

Acknowledgments

I would like to express my deepest gratitude to Peter Raboin, my company supervisor, for being a great mentor over the past three years. I thank him for the patience, insight, and much appreciated optimism through the seemingly endless obstacles. I appreciate his always taking the time out of his hectic schedule to guide me through my work.

I am also very grateful to Professor Merton Flemings for supervising this thesis project. I thank him for all his advice and support.

I thank Professor Carl Peterson, my departmental reader, for taking the time to read and approve this thesis.

Thank you to everyone at Lawrence Livermore: Dale Schauer for all his help and support; Brad Maker and Art Shapiro for their help in my analysis work; Larry Sanford for always being there to help; and Barbara Kornblum for all her advice and support. Thank you also to everyone who have made my stay very enjoyable.

Most of all, I thank my family and friends for their advice and encouragement. In one way or the other, they have helped me bring this thesis to completion.

Winnie C. M. Leung

Winnie C. M. Leung

Table of Contents

List of Figures

1.0 INTRODUCTION

1.1 Background

For a casting process to be successful, the finished parts must be of sound strength and free from defects. Designing defect free cast-metal parts by experimental trial and error can be costly and inefficient. The motivation behind this project, undertaken by Lawrence Livermore National Laboratory (LLNL), is to develop the means to simulate casting processes on a computer. The ultimate goal of this project is to be able to use finite element analyses to predict the final shape and the probable existence of any defects in the castings. One application of interest is then to use such codes to predict the presence of hot tears in sand castings.

To assure that the finite element analysis of a casting procedure generates realistic predictions, the solidification process and material properties must be modeled properly. Many current thermal and mechanical finite element computer codes depend on the user to input the appropriate temperature-dependent parameters to model the many physical phenomena which occur during solidification.

1.2 Project Overview

The objective of the work presented here was to gain an understanding of how casting processes should be modeled for thermomechanical analysis using existing analytical tools. Because thermomechanical analyses have not been performed extensively before, many issues still needed to be addressed. As such, this thesis project consisted of several phases.

First, predictions from finite element mechanical analysis were compared with theoretical calculations. Results from a finite element analysis of the stresses and strains resulting from a simple cool down process are compared to those predicted by solid mechanics theory in order to confirm the validity of the numerical prediction. The closed form solution enabled assessment of the validity of the numerical predictions.

Next, a general approach to the thermal and mechanical models of a typical finite element casting analysis is presented. A method of modeling the transfer of heat across air gaps at metal-mold interfaces during solidification is presented. Also, a material constitutive model capable of predicting the flow strength of metals at melting range temperatures is developed.

Coupled thermomechanical analyses were then performed for a cup casting experiment. The modeling methods developed were utilized and analytical results were benchmarked against experimental results. By studying the discrepancies between numerical and experimental results, much insight to solidification modeling was gained.

Finally, thermal and mechanical analyses were applied to a study of hot tears. A finite element model was created for an experiment used to produce hot tear specimens. Analyses were performed so that stress concentrations within the casting could be observed. A simplified hot tear design was created so that the analyses can be performed much more efficiently. Numerical analyses provided insight as to why past experiments had been unsuccessful.

In this thesis, each of these efforts is discussed in a chapter. In addition, information regarding the properties and parameters used in the finite element models is provided in the appendices so that the reader can repeat or modify the analyses if so desired.

2.0 VALIDATION OF MECHANICAL ANALYSIS RESULTS

Prior to using existing finite element codes to perform mechanical analyses for complicated models, a test problem was created for which stress predictions can be obtained from solid mechanics theory for comparison to finite element results. The closed form solution enabled assessment of the validity of the numerical predictions.

2.1 Test Problem

The stress distribution in a shrink-fit tube during cool down was predicted by theoretical calculations and also by finite element analysis. The problem was modeled as a steel cylinder surrounded by an outer ring of aluminum. (See Figure 1.)

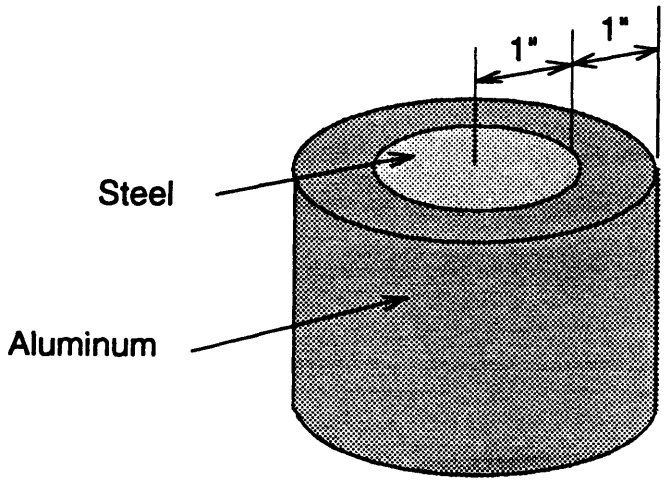

FIGURE 1. Steel and aluminum shrink fit tube assembly.

	Aluminum	Steel
Young's Modulus [psi]	10E+06	30E+06
Poisson's ratio	0.33	0.29
coef. of thermal expansion [°C]	11E-06	6E-06

TABLE 1. Aluminum and steel material properties used in analyses.

The entire part was cooled from 300 °C to 100 °C. The part was modeled as being constrained on the top and bottom surfaces so that there can be no axial displacements. The aluminum and steel properties used in the analyses are shown in Table 1. Since the coefficient of thermal expansion for aluminum is greater than that for steel, the outer aluminum annulus will experience more shrinkage than the inner steel core. The resulting constraint will impose stresses on the entire part. Although this test problem is very simple, it is representative of thermal stress problems which can arise in casting processes.

2.2 Theoretical Solution

A theoretical prediction to the distribution of stresses can be obtained by starting with the stress-strain relations expressed by Hooke's Law:

$$\sigma_r = \nu(\sigma_\theta + \sigma_z) + E(\varepsilon_r - \alpha\Delta T) \quad \text{(EQ 1)}$$

$$\sigma_\theta = \nu(\sigma_r + \sigma_z) + E(\varepsilon_\theta - \alpha\Delta T) \quad \text{(EQ 2)}$$

$$\sigma_z = n(\sigma_r + \sigma_\theta) + E(\varepsilon_z - \alpha\Delta T) \quad \text{(EQ 3)}$$

where E is Young's Modulus, ν is the poisson ratio, σ is the stress, and ε is the strain. The radial, hoop, and axial components of the stresses and strains are designated by the subscripts r, θ, and z respectively. Since the assembly is contrained to prohibit axial displacements, we have a state of plane strain, or $\varepsilon_z = 0$. Using this condition, Eqn. 1 can be simplified to the form:

(EQ 4)

$$\varepsilon_r = (1+\nu)\alpha\Delta T + \left[\frac{1-\nu^2}{E}\right]\left[\sigma_r - \frac{\nu}{1-\nu}\sigma_\theta\right]$$

Similarly, Eqn. 2 can be written as:

(EQ 5)

$$\varepsilon_\theta = (1+\nu)\alpha\Delta T + \left[\frac{1-\nu^2}{E}\right]\left[\sigma_r - \frac{\nu}{1-\nu}\sigma_\theta\right]$$

Expressions for the radial and hoop stresses can then be obtained by combining Eq. 4 and Eq. 5.

(EQ 6)

$$\sigma_r - \sigma_\theta = \frac{E\left[\varepsilon_r - \varepsilon_\theta\right]}{1+\nu}$$

(EQ 7)

$$\sigma_r = \frac{E(1-\nu)}{(1-2\nu)(1+\nu)}\left[\left[\varepsilon_r + \frac{\nu}{1-\nu}\varepsilon_\theta\right] - \alpha\Delta T\left[\frac{1+\nu}{1-\nu}\right]\right]$$

These two expressions are useful in rewriting the equation for radial force equilibrium:

(EQ 8)

$$\frac{d\sigma_r}{dr} + \frac{\sigma_r - \sigma_\theta}{r} = 0$$

as an equation in terms of the strains:

(EQ 9)

$$\left[\frac{1-\nu}{1-2\nu}\right]\left[\frac{d\varepsilon_r}{dr} + \left[\frac{\nu}{1-\nu}\right]\frac{d\varepsilon_\theta}{dr} - \alpha\left[\frac{1+\nu}{1-\nu}\right]\frac{d}{dr}\Delta T\right] + \frac{\varepsilon_r - \varepsilon_\theta}{r} = 0$$

Eq. 9 can then be further simplified into a form which can be solved easily by using the strain-displacement equations:

(EQ 10)

$$\varepsilon_r = \frac{du}{dr}$$

(EQ 11)

$$\varepsilon_\theta = \frac{u}{r}$$

where u is the radial displacement. Recognizing also the fact that $d\Delta T/dr = 0$, Eq. 9 can be expressed as a differential equation for u(r):

(EQ 12)

$$\frac{d^2u}{dr^2} + \frac{1}{r}\frac{du}{dr} - \frac{u}{r^2} = 0$$

which has a general solution of the form:

(EQ 13)

$$u = \left[\frac{C_1}{2}\right]r + \frac{C_2}{r}$$

where C_1 and C_2 are constants of integration. Substituting this solution into the strain-displacement equations, the strain in the hoop and axial directions can be expressed as:

(EQ 14)

$$\varepsilon_\theta = \frac{u}{r} = \frac{C_1}{2} + \frac{C_2}{r^2}$$

(EQ 15)

$$\varepsilon_r = \frac{du}{dr} = \frac{C_1}{2} - \frac{C_2}{r^2}$$

These two equations can then be substituted into Eqs. 6 and 7 to obtain equations for the radial stress and hoop stress distributions.

(EQ 16)

$$\sigma_r = \left[\frac{E}{(1-2\nu)(1+\nu)}\right]\frac{C_1}{2} - \left[\frac{E}{(1+\nu)}\right]\frac{C_2}{r^2} - \frac{E\alpha\Delta T}{(1-2\nu)}$$

(EQ 17)

$$\sigma_r = \left[\frac{E}{(1-2\nu)(1+\nu)}\right]\frac{C_1}{2} + \left[\frac{E}{(1+\nu)}\right]\frac{C_2}{r^2} - \frac{E\alpha\Delta T}{(1-2\nu)}$$

In order to obtain the stress distributions in the steel and aluminum, the four unknowns $C_{1,steel}$, $C_{2,steel}$, $C_{1,alum}$, and $C_{2,alum}$ must be found. The value of the constants can be found by considering the requirements imposed by the geometric constraint and boundary conditions. The boundary conditions are $\sigma_{r,steel} = \sigma_{\theta,steel}$ in the center (r = 0); $\sigma_{r,alum} = 0$ on the outer surface at $r = r_2$; and $\sigma_{r,alum} = \sigma_{r,steel}$ at the interface at $r = r_1$. Also, at the interface, geometric constraint requires that $u_{alum} = -u_{steel}$.

Upon solving the four equations generated by the constrains and substituting in values for the material properties, the following equations can be obtained for the stress distributions: (The unit of psi is used for the stresses and inch is used for radial position.)

- In the aluminum outer ring:

$$\sigma_{r_{alum}} = 2.186\times10^{3} - 8.729\times10^{3}\frac{1}{r^2} \quad \text{(EQ 18)}$$

$$\sigma_{\theta_{alum}} = 2.186\times10^{3} + 8.729\times10^{3}\frac{1}{r^2} \quad \text{(EQ 19)}$$

- In the steel core:

$$\sigma_{r_{steel}} = \sigma_{\theta_{steel}} = -6.536\times10^{3} \quad \text{(EQ 20)}$$

(Closed form solutions in terms of the material properties and geometric parameters are not provided here because they are too complex algebraically.)

2.3 Finite Element Analysis

The stress distributions were then predicted using finite element modeling. The mechanical analysis was performed using NIKE3D[1]. The finite element model of the part was generated using INGRID[2]. The mesh, shown in Figure 2, was generated for a quarter slice of the cylindrical part. It contains 11358 nodes and 5539 elements. The mesh was finely graded to achieve higher accuracy in the numerical results. Displacements were restrained on the two vertical planes of symmetry and on the top and bottom surfaces. The analysis was set to run for twenty time states. A temperature load curve with 300 ^{o}C in the initial time state and 100 ^{o}C in be final time state was applied to the mesh.

Mechanical analysis was then performed by NIKE3D to obtain distributions of radial stress and hoop stress within the part. Initially, analyses were performed with no sliding surface applied to the interface so that there can be no relative motion between the two materials. Subsequently, the analyses were repeated with a sliding interface so that the two materials can deform independently. The two cases yielded identical answers as is expected since the cooling processes does not induce any gap formation.

Although this problem can actually be treated as a two-dimensional linear-elastic plane strain problem which can be solved in one time step, it was solved as a three-dimensional problem in twenty time steps to better resemble the structure of more complicated analyses.

---

1. NIKE3D is a nonlinear, implicit, three-dimensional finite element code for solid and structural mechanics. It is supported by LLNL.
2. INGRID is a three-dimensional mesh generator supported by LLNL.

2.4 Comparison of Results

Stress predictions by NIKE3D are plotted against those predicted by Eqs. 18, 19, and 20. The radial stress and hoop stress distributions are shown in Fig. 3 and 4, respectively. It can be seen that the results are in very good agreement.

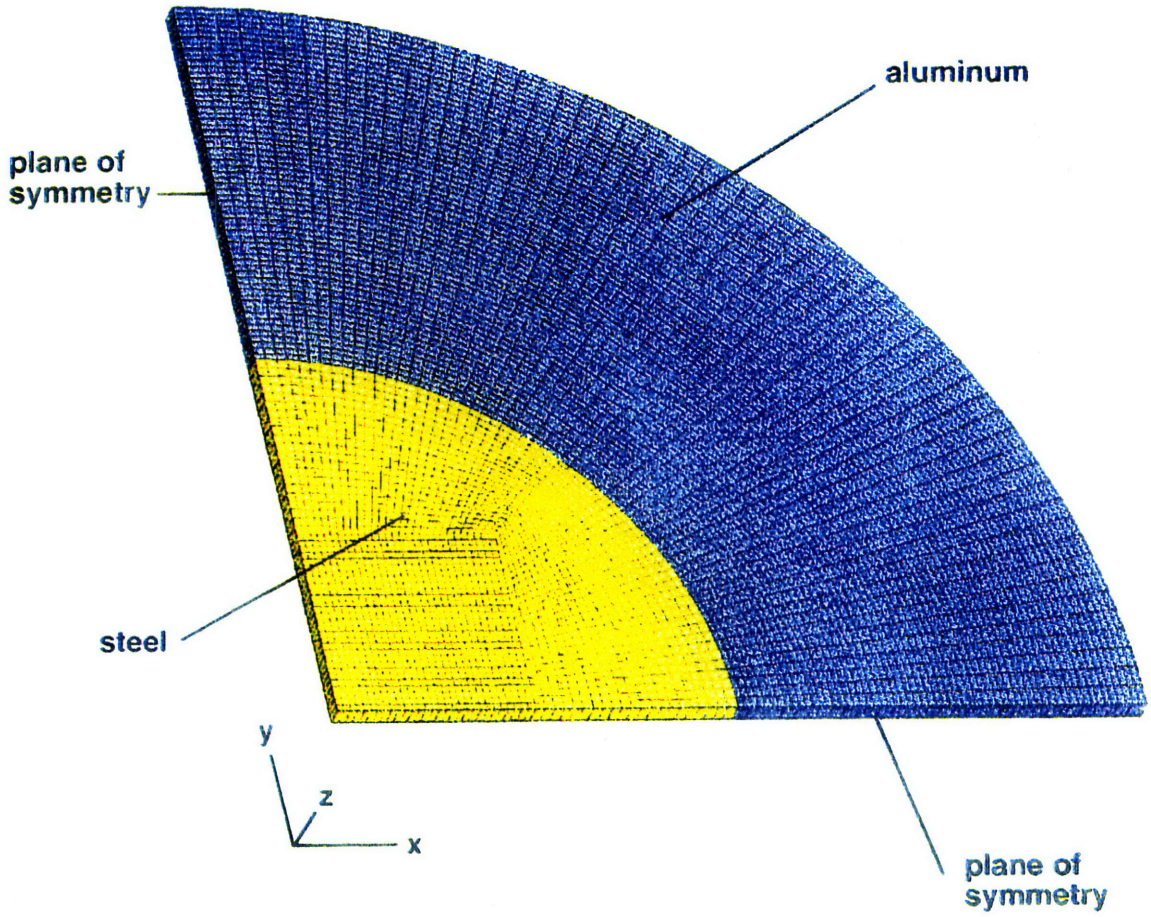

FIGURE 2. Finite element mesh for steel and aluminum part.[3]

3. Taken from "'Comparison of ProCAST with NIKE3D for Concentric Cylinder Thermal Stress Test Problem" by Barbara Kornblum and Winnie Leung. LLNL Memo, October 1994.

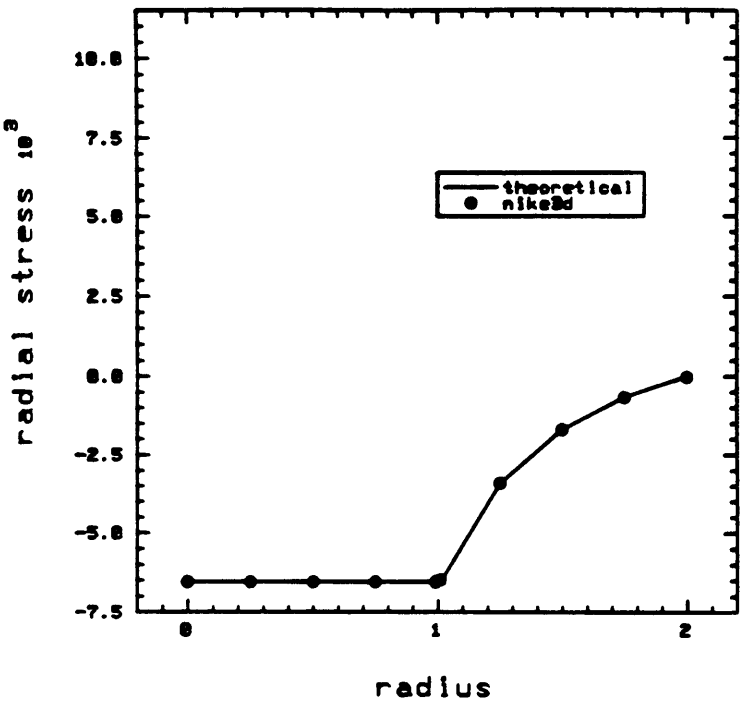

FIGURE 3. Comparison of radial stress distributions

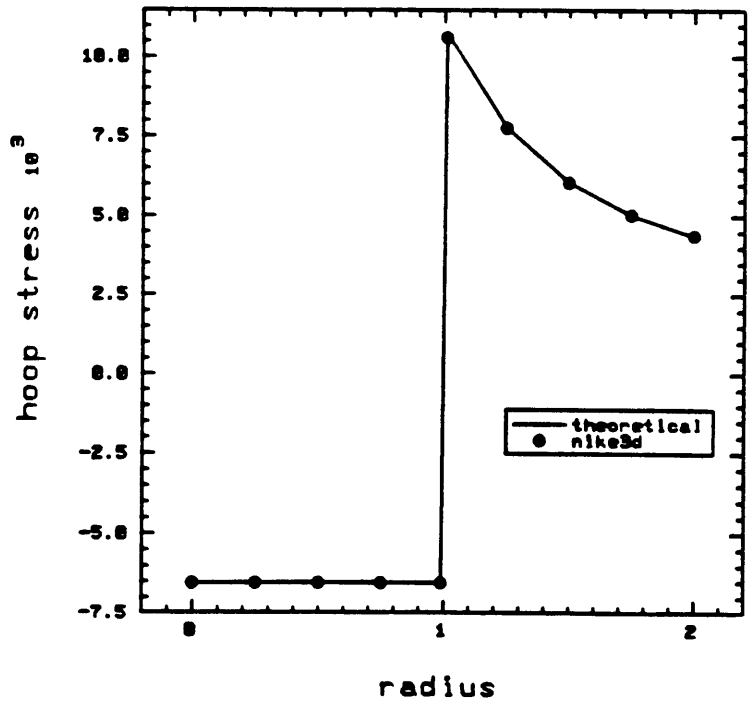

FIGURE 4. Comparison of hoop stress distributions

3.0 MODELING OF CASTING PROCESS

For analyses of casting procedures, models which can adequately describe the involved thermal and mechanical processes are essential to obtaining reliable results. There are two common difficulties in performing thermomechanical analyses of solidification processes. First, the formation of air gaps at metal-mold interfaces during solidification needs to be modeled to obtained the correct thermal response of the system. This effort is often complicated by the lack of understanding of the predominant modes of heat transfer across the gap. Second, a material constitutive model capable of predicting the liquid-solid mechanical behavior of metals needs to be developed. This problem is complicated by the fact that mechanical property data at high temperatures are usually not available, especially for metal alloys.

In this chapter, a general approach to the thermal and mechanical models used in the finite element casting analyses is described. The attempt to address the gap formation and material constitutive models is also discussed.

3.1 Thermomechanical Approach

The limiting capability of past technologies had dictated that thermal and mechanical analyses of solidification processes be performed in an uncoupled manner. That is, the thermal problem is solved for a fixed geometry, and then the temperature results are used as inputs to the mechanical problem. This approach neglects the effects of the mechanical response on the thermal problems. In problems where thermal contact is a significant factor, the uncoupled thermal and mechanical analyses will provide only

approximate solutions. For casting processes, where the formation of air gaps at metal-mold interface significantly diminish the transfer of heat, the coupled thermomechanical approach is likely to provide better solutions.

Recently, LLNL has developed a coupled thermomechanical code PALM2D which combines the thermal analysis traditionally performed by TOPAZ2D[4] and mechanical analysis by NIKE2D. In PALM2D[5], the thermal response of an initial time step is found and used to solve for the mechanical response. In turn, the thermal response at the subsequent time step is solved for the geometry determined by the mechanical analysis of the previous time step. The mechanical response is then found for the second time step and the process continues. This coupled approach allows for better predictions as the thermal analysis is now performed for a deforming geometry.

The thermomechanical approach to analyzing casting processes allows for predictions of phenomena which are thermally and mechanically related:

- Model the modes of heat transfer across casting-mold interfaces
- Model the mechanical behavior of metal near melting range temperatures
- Obtain predictions of temperature history and solidification time
- Predict the final shape of solidified castings and any interface gaps

3.2 Thermal Model

Many finite element analysis codes model thermal phenomena through time-dependent or temperature-dependent values of relevant parameters supplied by the users.

4. TOPAZ2D is a heat transfer finite element analysis code supported by LLNL.
5. PALM2D is a LLNL supported finite element analysis code which uses the staggered step approach.

Thus, it is very important to be able to identify the significant thermal conditions and to supply the appropriate modeling parameters.

3.2.1 Boundary Conditions

Convection and radiation boundary conditions can be applied to the exposed surfaces in the thermal analyses to model heat lost to the surroundings. The equation used for the convection boundary condition is:

(EQ 21)

$$q = h_c[T - T_{amb}]^a[T - T_{amb}]$$

where h_c is the convective heat transfer coefficient, T_{amb} is the ambient temperature, and a is the free convection exponent. For the radiation boundary conditions, the equation for radiation heat transfer was used:

(EQ 22)

$$q_r = \varepsilon\sigma\left[T^4 - T_{amb}^4\right]$$

where ε is the emittance and σ is the Stefan-Boltzmann constant.

3.2.2 Modeling the Specific Heat, C_p

In the thermal analysis, the specific heat of a metal is supplied by temperature-dependent data. Such data are usually available for common pure metals. The thermal properties for most specific alloys, however, have not been well established. A model of an alloy C_p data can be created by modifying that for its base metal. The specific heat values at low temperatures are usually known for most alloys. If high temperature data are not available, then the assumption that the base metal and its alloys have similar specific heat values at melt temperatures is made.

For analyses of metal solidification processes, the heat effects due to phase changes must be modeled. In TOPAZ, this is achieved by modifying the specific heat data to account for the heat of fusion, Δh_f. The amount of latent heat present can be integrated into the C_p curve since the latent heat can be defined as:

(EQ 23)

$$-\int_{T_l}^{T_s} C_p dT = \Delta h_f$$

where T_s is the solidus temperature and T_l is the liquidus temperature. This is also shown graphically in Figure 5. The area of the jump in the curve is equal to Δh_f. While the latent heat is actually released at the phase change temperature, it is advisable that the width of the spike not be made too narrow. If the width of the jump is smaller than the time step used in the finite element analysis, the latent heat will be overlooked if the interval should lie between two time steps.

For pure metals, the jump can take on any shape. For alloys, however, the heat of fusion at any temperature in the freezing range corresponds to the fraction solid, f_s, at that temperature such that:

(EQ 24)

$$\frac{-\int_{T_l}^{T} C_p dT}{-\int_{T_l}^{T_s} C_p dT} = f_s$$

Such a model will generate a curve with several peaks at the phase transformation temperatures.

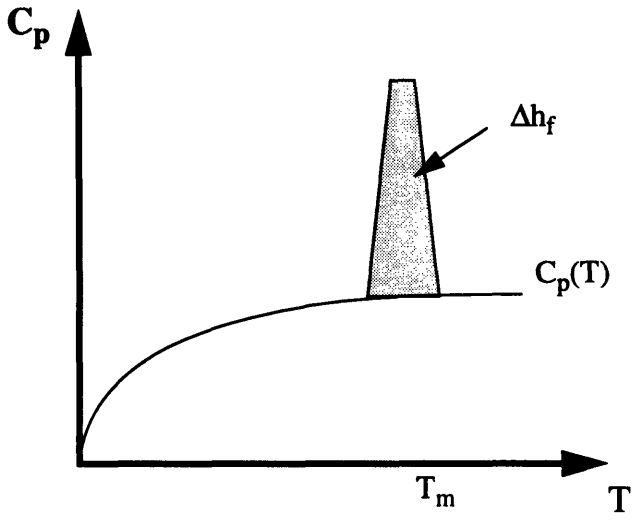

FIGURE 5. Integrating C_p value into the specific heat curve.

3.2.3 Modeling the Conductivity, k

The conductivity of a metal is also supplied by temperature-dependent data. Similar to the method used to create the specific heat model, the conductivity data is taken from literature whenever possible. The model is then completed using data for the base metal as an estimate.

In addition, the model can be further modified to simulate the effects of natural convection within the liquid metal in the very early stage of solidification. Convection occurs as the hotter liquids expand and rise while the cooler liquids contract and sink. This effect essentially sets up a circulation within the liquid, mixing the regions of different temperature. This natural phenomenon, however, is not simulated in Lagrangian finite element analyses. Therefore, unrealistically high thermal gradients might be predicted

within the casting. To remedy this situation, the value of the conductivity of the metal above the melting temperature can be increased by a factor of 5 to 10 in order to decrease the extreme temperature gradients which might be otherwise predicted. This modeling trick is unlikely to lead to any erroneous thermal response of the system since the value of K is increased only when the metal is still liquid.

3.2.4 Modeling of Heat Transfer Mechanisms Across Metal-Mold Interface

When a casting melt is first introduced into a cold mold, heat is transferred between the two by means of simple liquid-solid conduction. As the casting starts to cool, a solidifying shell forms and can contract away from the mold. At the same time, the mold surface increases in temperature and expands. The thermal expansion and contraction lead to the formation of interface gaps, causing the conduction through solid contacts to become negligible. A large drop in the amount of heat transfer across the gap is observed as the predominant mode of heat transfer changes from solid-solid conduction to convection through the gases in the gap. To model the change in heat transfer for finite element analysis, a load curve can be used to estimate the relationship between the heat transfer coefficient across the gap and the size of the gap. Also, a gap radiation multiplier can be used to model the effects of radiation.

As the contact between the casting and the mold diminishes, the conduction of heat through the gases within the interface gaps becomes the predominant mechanism of heat transfer. In modeling the correlation between heat transfer coefficient and gap size, dimensional analysis can be used to find the relationship:

(EQ 25)

$$h \propto \frac{k}{d}$$

where h is the heat transfer coefficient, k is the overall conductivity of the gases inside the gap, and d is the gap width. Using this relationship, a curve can be determined for h at different widths as the gap formation progresses. As h is inversely proportional to d, its value approaches infinity as the gap size approaches zero. Thus, a physical upper limit must be applied for the value of h when no gap is present. The heat transfer can then be expressed by:

(EQ 26)

$$q = h\Delta T$$

where q is the heat flux and ΔT is the temperature difference across the gap.

It is worthwhile to note the importance of recognizing the approximate make-up of the gases inside the gap. For instance, hydrogen is a common component in mold gases. The thermal conductivity of hydrogen is approximately 7 times higher than that of air. Thus, neglecting to correctly identify the gap gases can lead to a significant error in the heat transfer coefficient model.

As the gap forms between the mold and casting, radiation heat transfer becomes more significant. This mode of heat transfer can be described by:

(EQ 27)

$$q_r = \varepsilon\sigma\left[T_1^4 - T_2^4\right]$$

where q_r is the heat flux from radiation, ε is the emittance, σ is the Stefan-Boltzmann constant, and T_1 and T_2 are the temperatures on opposite sides of the gap, such that $(T_1 - T_2)=\Delta T$. This equation can also be expressed in the form of Eq. 10:

(EQ 28)

$$q_r = h_r \Delta T = \left[\varepsilon\sigma\left[T_1^2 - T_2^2\right]\left[T_1 + T_2\right]\right]\Delta T$$

where $[\varepsilon\sigma(T_1^2-T_2^2)(T_1+T_2)]$ is defined as the radiation multiplier. By comparing the values of the h in Eq. 9 and the radiation multiplier, one can determine whether the effects of radiation are negligible.

It should be noted that the significance of radiation heat transfer varies from case to case. Two experimental findings were cited by Campbell in his work. [Campbell, 1991] For the casting of light alloys, radiation effects are negligible as the amount of heat transfer across the air gap by radiation is generally only of the order of 1 percent of that due to conduction by gas. [Ho and Pehlke, 1984] However, for higher temperature metals, such as the casting of steels in different gases or in vacuum, radiation heat transfer becomes increasingly significant. [Jacobi, 1976]

3.2.5 Modeling of Material Interface

In TOPAZ finite element thermal analysis, the application of a thermal interface slideline allows an interface heat transfer coefficient to be defined. Furthermore, the presence of a slideline allows adjacent elements of different materials to be assigned their own distinct initial temperatures. Without a slideline, adjacent elements of different materials at the interface will be assigned a temperature gradient to transition the difference in temperature. While a transition in adjacent temperatures can allow for easier convergence of a thermal solution, neglecting to assign a thermal slideline can result in a significant temperature profile. This point is demonstrated graphically in Figure 6.

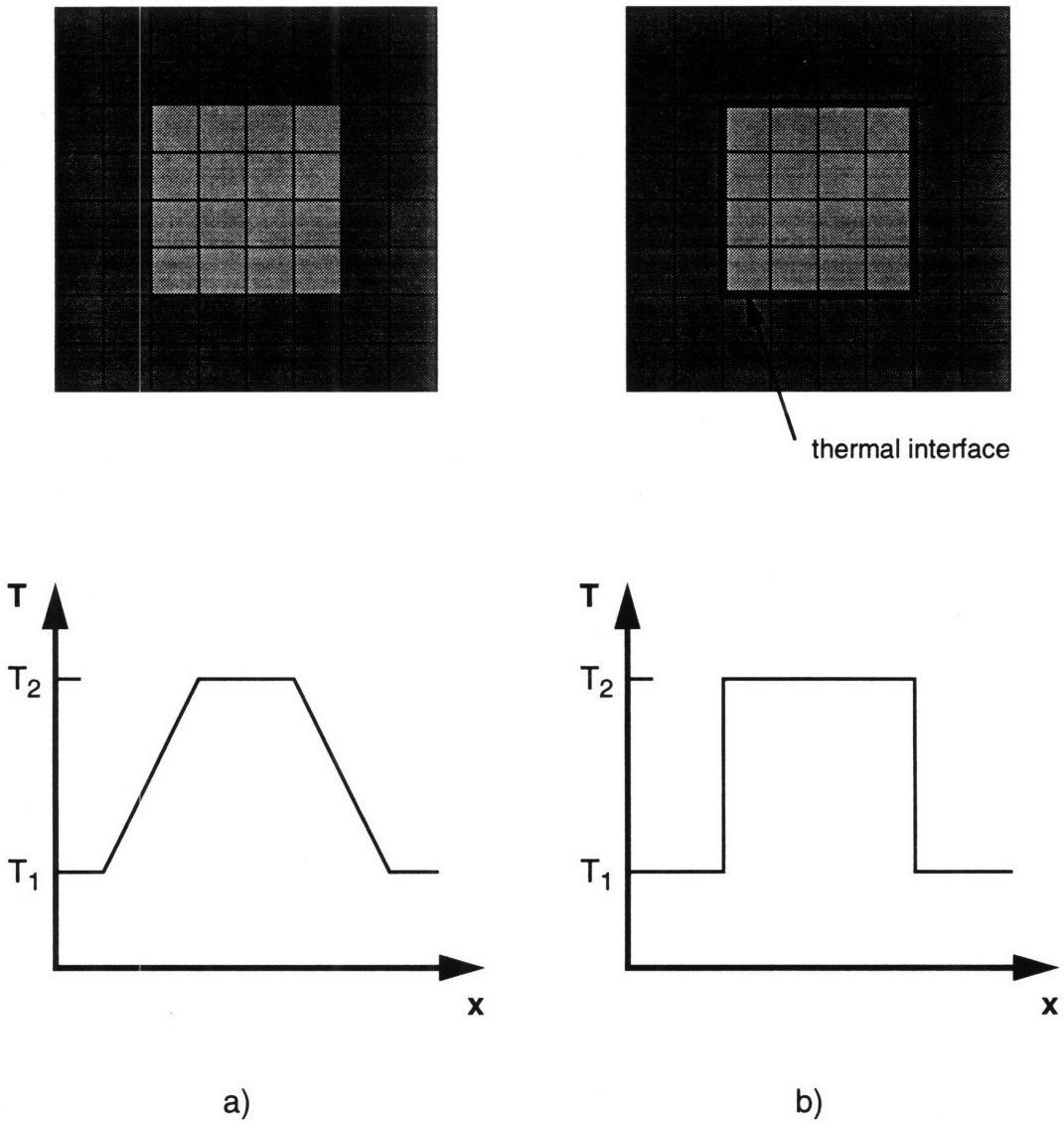

FIGURE 6. Initial temperature profiles of example a) without and b) with interface slideline.

3.3 Mechanical Model

Mechanical analyses were performed using a new solidification constitutive model currently being developed at LLNL. We have begun studying creep behavior to understand how metal behaves at high temperature as it experiences stresses. We have also set up a method to model the temperature dependency of metal density.

3.3.1 Temperature Dependency of Density

The changes in density associated with the phase transformations can be modeled by the thermal expansions and contractions using the metal's secant coefficient of thermal expansion (CTE) at different temperatures. As phase transformations occur, a metal's CTEs vary as it experiences thermal expansions or contractions. A set of temperature-dependent CTE values needs to be determined. First, density data as a function of temperature is needed. The density, ρ, can then be derived as a function of the thermal strain by using the basic relationship of ρ = Mass / Volume. As the material experiences the rise in temperature, its density decreases as it expands. Thus, the density, ρ^T, at a higher temperature can be determined by:

(EQ 29)

$$\rho^T = \frac{M}{\left[1+\varepsilon^T\right]^3 V_0}$$

The temperature dependency of density can then be expressed as:

(EQ 30)

$$\ln\left[\frac{\rho_0}{\rho^T}\right] = 3\ln\left[1+\varepsilon^T\right]$$

where ρ_o is the density at the reference temperature. Using Eq. 30, the thermal strain, ε^T, can be determined. The secant coefficient of thermal expansion, α, can then be obtained from the relationship:

$$\varepsilon^T = \alpha(T-T_{ref}) \qquad \text{(EQ 31)}$$

Note also that ε^T is defined to be zero at the reference temperature, T_{ref}, and the material is said to be in its stress free state.

3.3.2 Material Strength Constitutive Model

The modeling of a material's constitutive properties is difficult because of scarcity of information on the mechanical behavior of metals in the semi-solid state. While a metal's mechanical properties at low temperature is are readily obtainable, those for elevated temperatures near its melting range are usually not available. We studied how a metal behaves near its melting point in order to model its material properties. At high temperatures, metals show rate-dependent plasticity, or creep. Thus, the strength of liquid metal is modeled by predicting the stress resulting from different strain rates at varying temperatures. After determining the material strength at the extreme liquidus and solidus ranges, a transition between the high and low temperatures can be attempted.

In steady state creep (or secondary creep), the relationship between the steady state creep rate $\dot{\varepsilon}^p$, stress σ, and absolute temperature T, can be expressed as:

$$\dot{\varepsilon}^p e^{\frac{Q}{RT}} = A\sigma^n \qquad \text{(EQ 32)}$$

where Q is the activation energy for creep, $\overline{R}$ is the Universal Gas Constant, A is the creep constant, and n is the creep exponent. [Harper et. al., 1958] The values of the constants Q, A, and n are unique to each material, and have to be found experimentally. At low stresses, n has a value of about 1. At intermediate stresses, power law is observed and n typically has a value between 3 and 8.

For common metals, data from deformation mechanism maps can be used to set up the flow strength model. Unfortunately, such data are often not available for metal alloys. In such cases, models are created for alloys by using data for the low temperature strength. The mechanical behavior at melting range temperature is then modeled by using data for its base metal. Again, a transition is created by curve fitting the data for the low and high temperature regimes.

In the mechanical analysis code NIKE2D, a simplified and more robust form of Eq. 31 is used. Here, the deviatoric strain rate is approximated as the plastic strain rate. An equation of the following form is used:

(EQ 33)

$$\sigma = S\left[\frac{\dot{\varepsilon}}{A}\right]^{m}$$

where σ is the flow strength, A is the strength coefficient, S is the strength parameter, $\dot{\varepsilon}$ is the deviatoric strain rate, and m is the strain sensitivity. m can also be expressed as 1/n, where n is the strain exponent as defined in Eq. 31. S can be assigned different values to

model strain hardening effects. In our casting analysis, S has a value of 1 since no strain hardening behavior is expected.

In setting up the flow strength model, values of m and A are found by solving Eq. 33 using any existing strength data. Temperature-dependent data points for A and m are then inputted as load curves for the mechanical analysis. Since A and m are entered as discrete data points at the temperatures for which data were available, the strengths at these temperature will be given in the strength data. For temperatures in between the data points, a linear interpolation is made for the values of A and m. The corresponding flow strength value is then calculated. However, as indicated by Eq. 32, A is not linearly proportional to σ. Therefore, because of the exponential nature of the equation, there is not a smooth transition in the curve from one point to the next. This deviation from a smooth curve, however, can be minimized by increasing the number of data points for A and m.

Another modeling error introduced by our model is the over-estimation of flow strength caused by the simplification of m as being dependent only on the temperature. In reality, m is also dependent on the stress and the strain rate as indicated by Eq. 31. The error caused by this assumption is illustrated in Figure 7. Consider, for instance, the strength of the metal at a given temperature. In our model, the material has different strengths depending on the strain rate. However, m is modeled to be dependent only on temperature and does not change with the strain rate. Suppose that a value of $m=m_1$ was determined from the creep data for a small strain rate. While the value of m actually changes from m_1 to m_2 as the strain rate increases, m is assigned a constant value of m_1 in our model, resulting in a very large modeling error of e_1. This monstrous error is caused

by the large slope change as m changes from having a value of about 1 at low stresses to a value on the order of 100 at high stresses. Similarly, if data for a large strain rate was available, then the value of $m=m_2$ will be used in the strength model. The modeling error e_2 in this case is much less severe than e_1 for the former case.

Thus, the modeling error resulting from neglecting the strain rate and stress dependency of m can be minimized by determining a value of m from strength data for larger strain rates if they are available. This will minimize the error in the flow strength predictions for high strain rates at low temperatures. However, comprehensive sets of creep data are often not available, especially for specialized metal alloys. Fortunately, this modeling error is unlikely to have any significant effects in the analysis because the strain rates observed at low temperatures are typically very small once the casting has solidified.

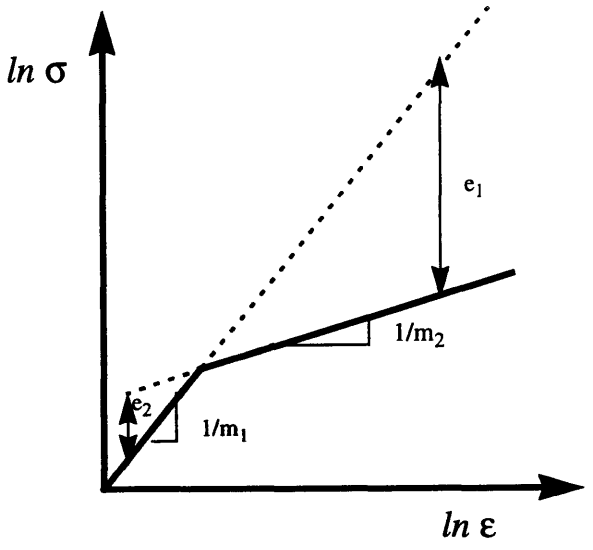

FIGURE 7. Variation of strain rate sensitivity with strain rate and stress

Another limitation of the current model is that a cut-off stress level has to be picked arbitrarily above which the value of the strength is modeled as remaining constant. Our constitutive model is only capable of predicting the strength while the material is still in the power law creep regime. For very high stresses, the model is no longer valid as the material will be deforming by a different mechanism.

Finally, it should also be noted that the strength predicted by this model is only a general approximation. In reality, the parameters of a casting procedure can greatly influence the strength of the finished parts. For instance, the finished products of sand casting and permanent mold castings will have different mechanical properties. Other factors such as grain size, feeding length, and cooling rate are also important.

4.0 BENCHMARKING OF FINITE ELEMENT RESULTS

In order to understand how casting procedures should be modeled for finite element analyses, ways to benchmark results from computer models must be available. Experimental casting results can be used as comparison with numerical results. For this purpose, experimental castings of aluminum in a steel cup were made. The thermal and mechanical responses of the system were observed and measured. Subsequently, the problem was modeled using finite element analysis. The finite element predictions were then compared to experimental data.

The availability of a benchmarking tool allowed assessment of the success of the thermal only and thermomechanical analyses. In addition, modeling approaches discussed in Chapter 3 were utilized and evaluated. The cup casting experiment was chosen as a benchmarking tool because it was simple to conduct. Also, the experiment can be accurately modeled using two dimensional finite element analysis. This is very important since the simplicity of the finite element model permits the analyses to be done more efficiently.

4.1 Cup Casting Experiment

The cup casting experiment was part of an on going research project at LLNL to model the solidification of metal castings. The experiment involved simply pouring molten metal into a cylindrical steel cup. The mold was formed by welding a cylindrical piece to a flat base piece. In a first experiment, pure Aluminum was poured at 730 ^{o}C into an unheated cup at 27 ^{o}C. A second experiment was performed where Aluminum 319 was

poured at 757 °C into the mold at 25 °C. Upon solidification, the assembly was sawn apart so that the cross section can be observed.

A cross sectional diagram of the casting assembly showing its dimensions is shown in Figure 8. Thermocouples were placed throughout the casting to collect temperature history data as the metal solidified. Linear-variable differential transformers (LVDTs) were also used to capture any displacements as the casting cooled and contracted. In the first experiment in which pure Aluminum was used, the thermocouples were inserted horizontally. The position of the thermocouples is shown in Figure 9a. During the experiment, it was observed that the thermocouples inhibited the shrinkage of the casting as it cooled. Therefore, in the second experiment in which Al 319 was used, the thermocouples were inserted vertically. The new position of the thermocouples is shown in Figure 9b.

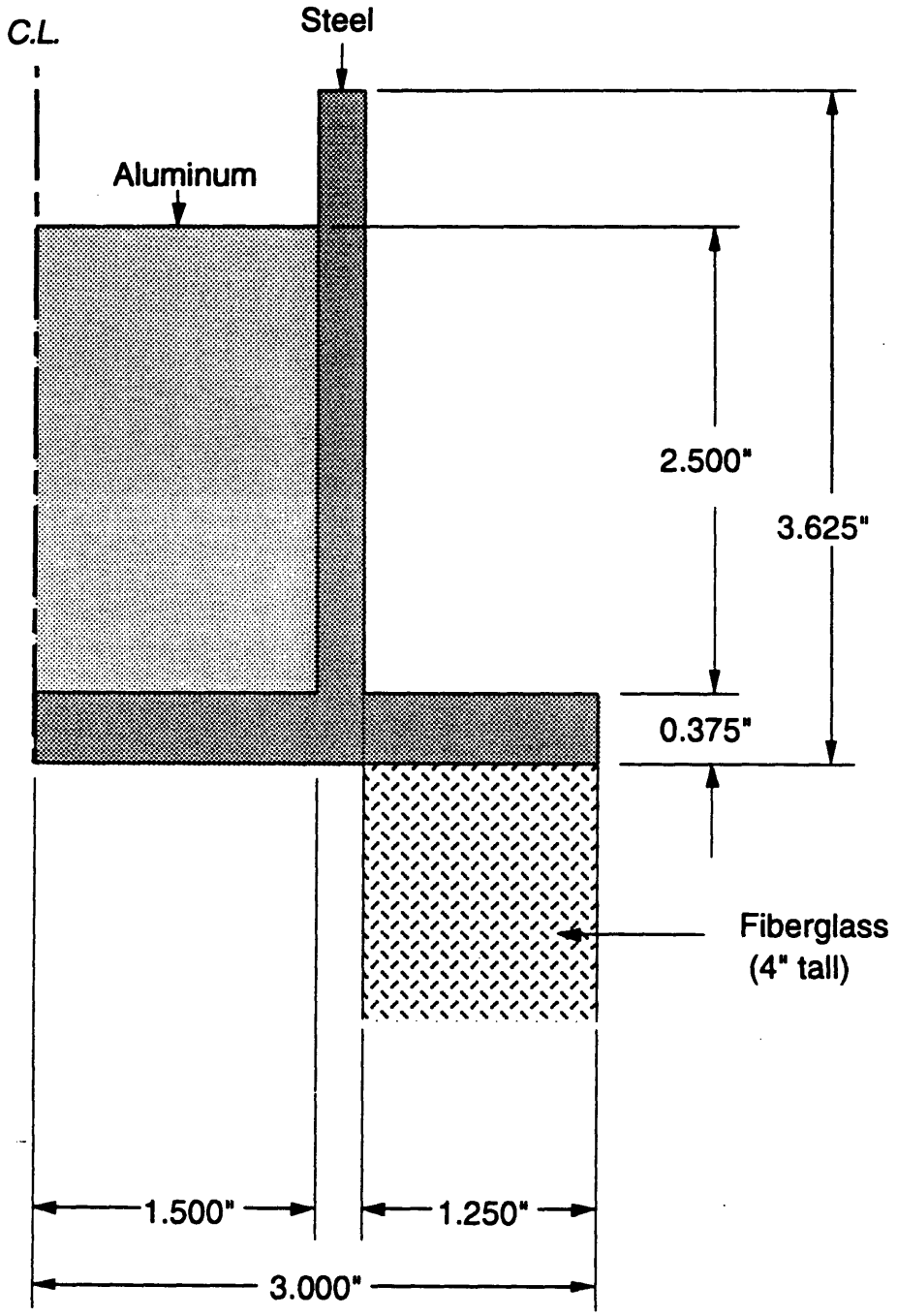

FIGURE 8. Cross sectional diagram showing dimensions of aluminum casting assembly.

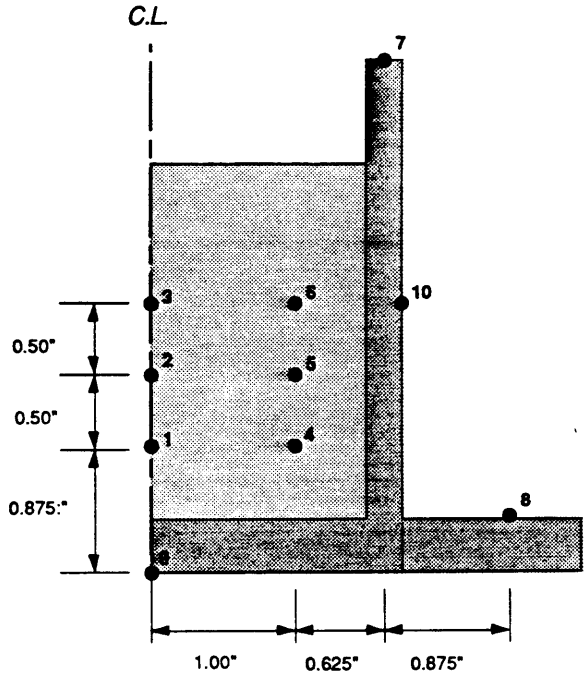

a)

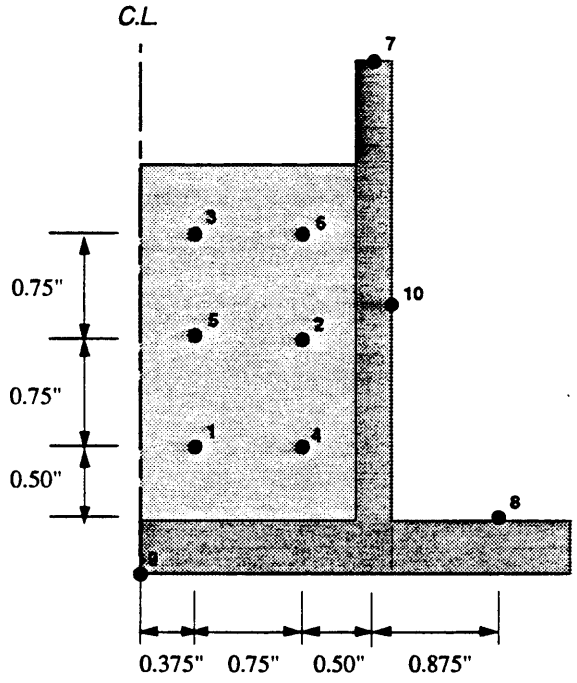

b)

FIGURE 9. a)Position of thermocouples for aluminum experiment; b)Position of thermocouples for aluminum 319 experiment.

4.2 Finite Element Model

A finite element model of the casting experiment was created. Since the problem is axially symmetric, only a two dimensional cross section need be modeled. The mesh, generated using MAZE, is shown in Figure 11. The mesh contains 1967 nodes and 1775 elements. Thermal analyses were performed using TOPAZ2D. Coupled thermomechanical analyses were performed using PALM2D. The thermomechanical approach was discussed in Section 3.1.

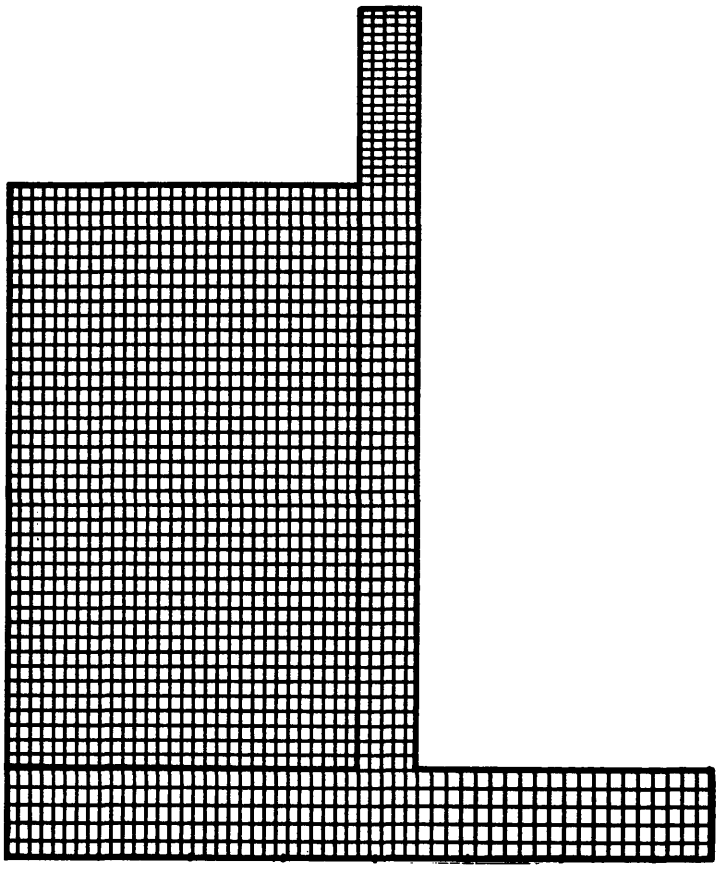

FIGURE 10. Finite element mesh of cup casting assembly

4.2.1 Thermal Solution

In our model, the melt surface and the cup's outer surfaces were cooled by convection and radiation heat loss to an ambient temperature of 25 ^{o}C. The convection boundary condition was modeled by Eq. 21. The convective heat transfer coefficient, h_c, was approximated to be 1 Btu/hr-ft^2-^{o}F (5.6786 W/m^2-^{o}K). The free convection exponent, a, was chosen to be 0.25, which is the free convection exponent for laminar air flow over vertical or horizontal plates. Radiation heat transfer was modeled by Eq. 22. A value of 0.7 was used for the emittance in the equation for radiation heat transfer. In addition, an adiabatic boundary condition was assigned to the section at the base of the cup which was supported by a thick fiber glass block.

In the thermal only analyses, thermal conduction between the casting and the mold is assumed since the analyses assumes a fixed geometry. A thermal slideline was assigned at the casting-mold interface and the interface heat transfer coefficient was approximated as 1000 W/m^2-^{o}K.

In the coupled thermomechanical analyses, the transfer of heat across interface gaps was modeled by the approach discussed in Section 3.2.4. A load curve was set up to model the gap heat transfer coefficient using Eq. 25. k was chosen to be 0.02414 W/m-^{o}K, which is the conductivity of air at room temperature. It is valid to assume that the gap formed at the interface consisted mostly of air since our experiment involved an open mold. In our analysis, a limiting value of h=10000 W/m^2-^{o}K was applied for a gap size of zero. This value was chosen as an order of magnitude estimate of the heat transfer coeffi-

cient in the presence of a perfect contact interface.[6] This high value of h is likely to be accurate only in the very early stage when the thermal contact is still excellent. In addition, radiation heat transfer across the gap was also modeled using Eq. 27. The emissivity was estimated to be about 0.85.

Thermal properties of pure Aluminum were available in literature and are shown in Appendix A. For Al 319, only the thermal properties at low temperatures were available.[7] The thermal data were then completed by approximating the thermal properties of Al 319 at melt temperatures to be the same as that for pure Aluminum. The thermal properties for Al 319 used in the thermal model can be found in Appendix B. Also, for both metals, the latent heat of fusion quantity was integrated into the specific heat curve as described in Section 3.2.2. The conductivity values were increased by a factor of 10 in the liquidus range to model the circulation of the cooling liquid metal due to natural convection.

4.2.2 Mechanical Solution

A mechanical interface slideline was applied between the cup and the casting so that the two can deform independently. Nodes along the center line were constrained in the horizontal direction to form the symmetry plane. Nodes along the bottom of the cup were constrained in the vertical direction to model the physical support. In addition, a downward body force was applied to model gravitational effects.

---

6. "Heat Transfer Data Book" by General Electric Company Corporate Research and Development. November 1970.
7. "Aluminum 319.0", Alloy Digest, May 1985.

The mechanical material properties of pure Aluminum and Al 319 can also be found in Appendix A and B. Such data were available only for lower temperatures. Near the liquidus ranges, the metal properties changes drastically as it becomes mushy and retains little strength. Using thermomechanical analyses, we studied the importance of strain rate dependence on the strength of the castings.

PALM2D analyses were first performed using a strain rate independent yield strength model. (Shown in Table B5 in Appendix B.) The values for the yield stress were determined by an "iterative" process. That is, initial values were chosen and the analysis was performed. The predicted approximate strain rate within the part was observed and the corresponding yield stress predicted by the rate dependent model was then used as the material yield strength for future analyses. This method is not always feasible though. The stresses predicted by the rate dependent model are typically too small to achieve convergence in the rate independent solution. The low strength caused the rate independent analyses to hourglass and deform wildly. Because of this numerical difficulty, the yield strength had to be made arbitrarily higher so that the solution would not diverge.

Subsequently, analyses were also performed using a strain rate dependent strength model using the approach which was described in Section 3.3.2. To construct the flow strength model for pure Aluminum, data from a deformation mechanism map were used. (Shown in Figure 11.) Eq. 33 was used to obtained the parameters necessary to create the model. (Repeated here in Eq. 34 for convenience.)

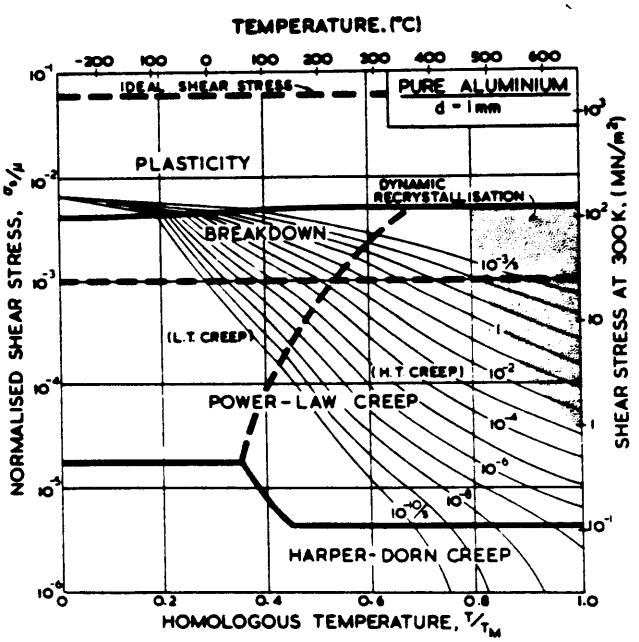

FIGURE 11. Deformation mechanism map for pure Aluminum.[8]

(EQ 34)

$$\sigma = S\left[\frac{\dot{\varepsilon}}{A}\right]^{m}$$

The values of m and A are used as inputs in the mechanical finite element code to determine the rate dependent strengths. A and m are entered as discrete data points at intervals of temperature. As discussed earlier, because of the non-linear nature of Eq. 34, increasing the number of data points will increase the smoothness of the flow strength curves generated.

The temperature-dependent values of m are determined by reading from the deformation mechanism map the strengths at two different strain rates for a given temperature. Substituting these values into Eq. 34, m can be determined by solving:

8. Taken from Frost and Ashby, 1982.

$$m = \frac{\ln[\sigma_1/\sigma_2]}{\ln\left[\frac{\varepsilon_1}{A_1}/\frac{\varepsilon_2}{A_2}\right]} \quad \text{(EQ 35)}$$

and approximating for now that A_1 equals A_2. After obtaining values for m, A can simply be determined by solving Eq. 34. A simple computer algorithm was then written which used the data points for m and A to generate the strain dependent models. Figure 12 shows such a plot of the flow strength model for pure Aluminum. Example curves are shown for the strain rates of 10^{-1}, 10^{-3}, 10^{-5}, and 10^{-7} per second.

The constitutive model for Al 319 was created similarly. Our efforts were complicated by the fact that we only had a few data points to base the model on. (Shown in Table 2.) Unfortunately, the data were also for extremely small strain rates, ($2.8x10^{-10}$ and $2.8x10^{-11}$ per second), making the model even less accurate.

Temperature [K]	Stress [psi] creep rate: 0.0001%/hr.	Stress [psi] creep rate: 0.00001%/hr.
373	25000	24500
422	20500	17500
477	13500	10000

Table 2. Creep Data for Aluminum 319.[9]

Values of m and A for Al 319 were then computed for the temperatures for which the creep data were available. Since the alloy has a melting range of 789 °K to 878 °K, the flow strength was approximated as that of pure aluminum above 650 °K. A transition

9. "Aluminum 319.0", Alloy Digest, May 1985.

between the two regimes was then found by approximating a curve fit. In addition, a cut-off in the stress level was imposed on the model beyond which our model is considered invalid. Figure 13 shows a plot of the Al 319 rate-dependent strength model. The data points used for m and A in the analysis are shown in Appendix B. It can be observed that m was found to have a value of about 1 at the liquidus temperature; 0.25 near the solidus, and only about 0.01 at room temperatures.

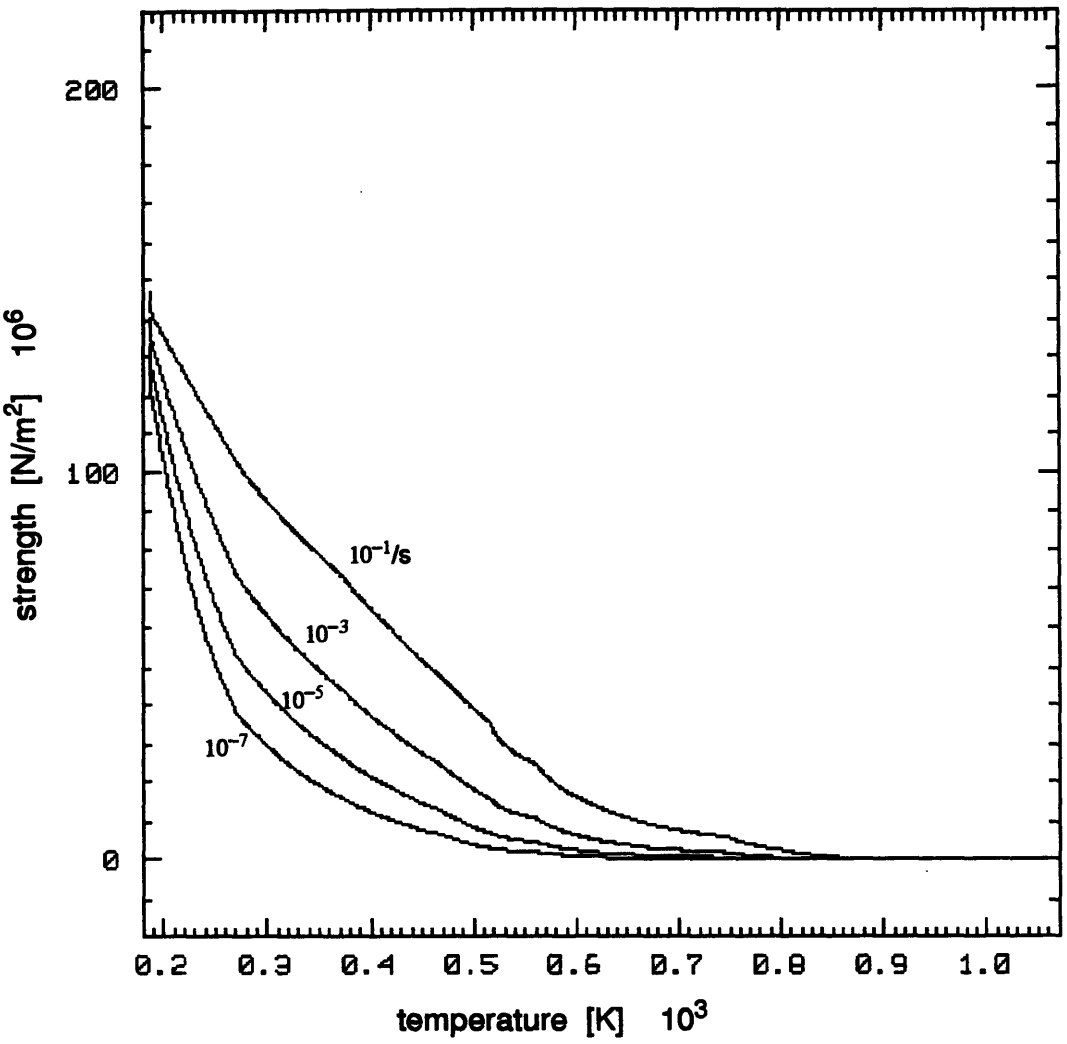

FIGURE 12. Strain-rate-dependent Flow Strength Model for Pure Aluminum

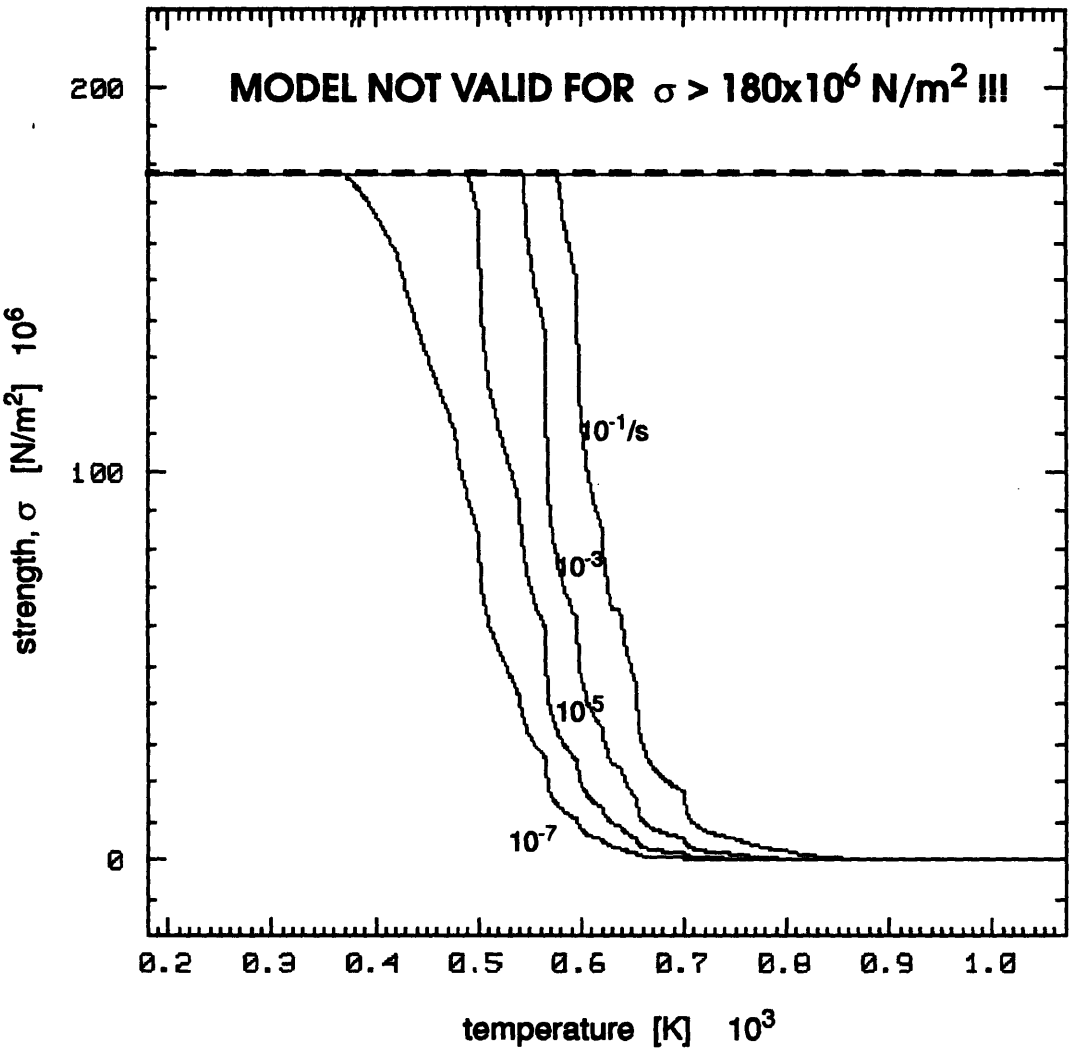

FIGURE 13. Strain-rate-dependent Flow Strength Model for Al 319.

4.3 Results

4.3.1 Solidification of Casting

Meshes detailing the deformation of the cooling casting are shown in Figure 14. Temperature fringe plots of the aluminum solidifying in the steel cup are shown in Figure 15. By studying these plots, the cooling process can be better understood.

In the early stages of solidification, the outer region of the aluminum casting begins to cool rapidly as it transfers heat to the cup. The top surface begins to drop near the cup as the casting contracts. A well defined gap forms along the side wall. On the bottom interface, small openings can be found near the axis. As solidification progresses, the outer region of the ingot has become solid and the inner core region continues to cool. A crater is formed on the top surface in the center as the core region cools and contracts. Once the entire casting has solidified, there is no longer any significant changes in shape and only small degrees of overall shrinkage are observed.

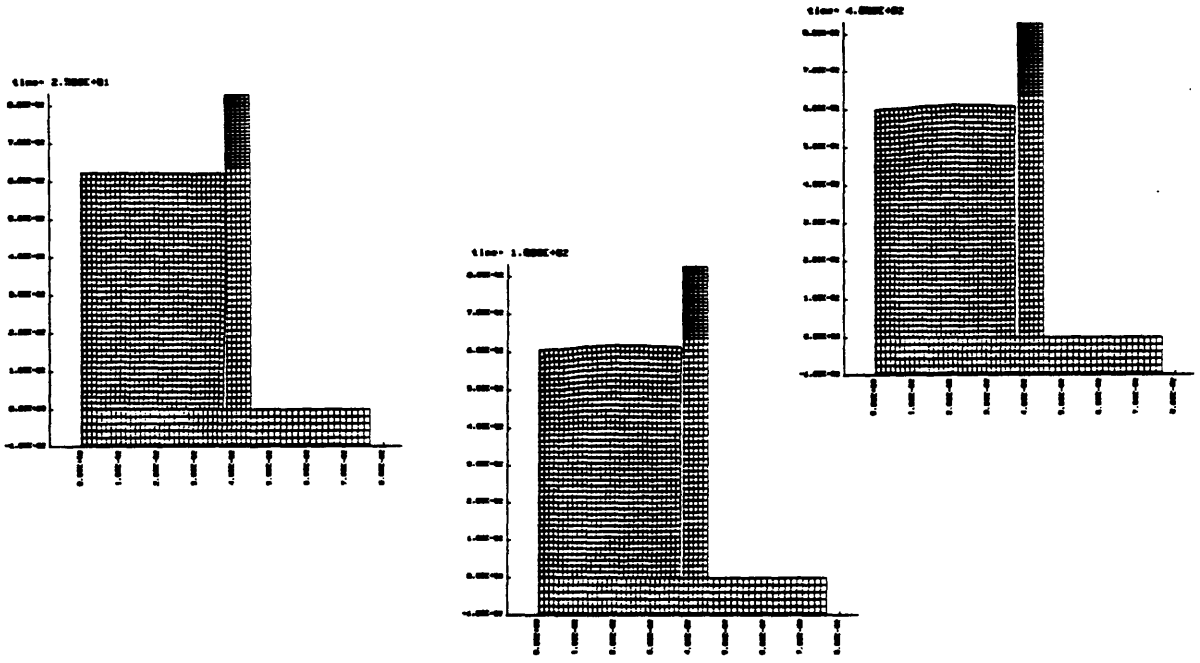

FIGURE 14. Meshes illustrating the shrinkage experienced by solidifying casting.

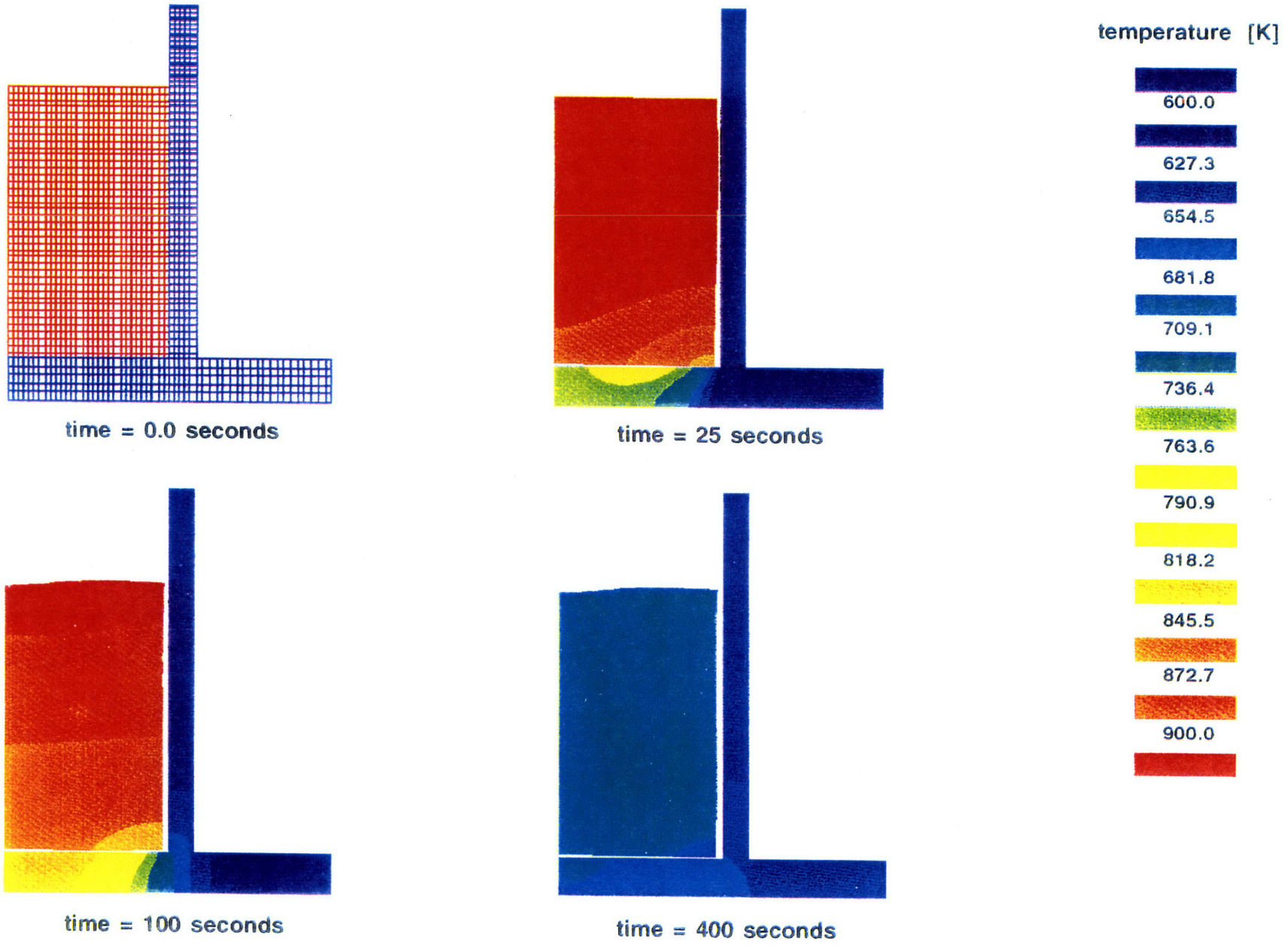

FIGURE 15. Temperature fringe plots of aluminum solidifying in steel cup.

4.3.2 Cooling Curves

The temperature history plots generated by the TOPAZ2D thermal only analysis of Al 319 is shown in Figure 16. The PALM2D thermomechanical analyses for Al 319 also generated cooling curves for the case with the strain rate independent flow strength model, which is shown in Figure 17. That for the rate dependent model is shown in Figure 18. By comparing these curves with the experimental thermocouple data, insight into the finite element models can be gained.

From these plots, it can be observed that the two thermomechanical analyses generated cooling curves which are about identical, with the rate depend model predicting just slightly lower cooling rates with the casting. The thermal only analysis with a constant interface of h = 1000 W/m^2-^oK, however, predicted cooling curves which showed more discrepancies with experimental results. In the early stages of solidification, the results are still comparable. As the gap forms at the casting-mold interface, however, the cooling rates decreases. From this point, the numerical cooling rates start to deviate from the experimental results because the constant-h model did not address the drop in heat transfer caused by the gap.

Furthermore, the curves in Figure 18a suggest that the value of h is higher than 1000 W/m^2-^oK initially. While the molten metal is still in good contact with the mold, much heat is rapidly transferred to the mold during the experiment, raising the mold temperature to as high as 550 ^oC in less than 20 seconds. This behavior is not predicted in the analyses. A comparison of the curves in Figure A clearly confirms the fact that the heat transfer across the casting-mold interface is indeed very high in the beginning. As solidi-

fication continues, however, the transfer of heat decreases as interface gaps form. Thus, h must take on values which change as solidification progresses in order to obtain better thermal results.

Figures 17a and 18a show that the thermomechanical analyses generate cooling curves within the casting which are in general agreement with the thermocouple readings. On closer inspection, however, discrepancies in the intrinsic properties of Al 319 can be noticed between those used in our finite element model and the actual properties of the experimental alloy. For instance, three noticeable steps which correspond to the phase transformation temperatures can be found in the cooling curves, However, the phase transformation temperatures used in our model, which were obtained from a previous experiment at LLNL, are different from those revealed by the experimental cooling curves. This may be caused by errors in the previous experiment used to determine the Al 319 fraction solid curve, or just simple material variations. By assuming that the experimental casting is completely solidified after the last noticeable phase transformation step, the casting took about 170 seconds to completely solidify. This solidification time is well predicted by the analysis with the rate-dependent strength model; and is just slightly over-predicted by the rate-dependent case at 200 seconds.

A comparison of the cooling curves also indicates that in our analyses, the casting remained very isothermal and the cooling curves lie very close together. In the experiment, however, the spread in the curves indicated a much bigger temperature gradient. One plausible explanation is the idealized conditions modeled in our analysis. While it actually takes about ten seconds to pour the molten metal into the steel cup, our analyses were simplified and the mold is assumed to be filled instantaneously. During the experi-

ment, however, the melt starts to solidify as soon as it splashes into the cup. Therefore, by the time all of the melt had been poured, a substantial temperature gradient might already exist.

By comparing the cooling curves for the steel cup, we can understand how well our model predicted the formation of gaps. Experimental data show that the thermocouple (#10) in the side of the cup rises to 550 ^{o}C before dropping as solidification continued. In our analysis, however, this sharp rise is not observed. After reaching only about 210 ^{o}C, a gap opens on the side interface and the cooling rate drops drastically. As a result, the cooling curve predicted at the rim of the cup (#7) is extremely low. On the other hand, the predicted cooling curve at the thermocouple (#9) on the bottom of the cup along the axis is in much better agreement. The analysis predicted a greater amount of heat being transferred to the bottom than the experimental results. This is consistent with the fact that our model predicted a gap at the bottom interface which is smaller than that observed in the experiment.

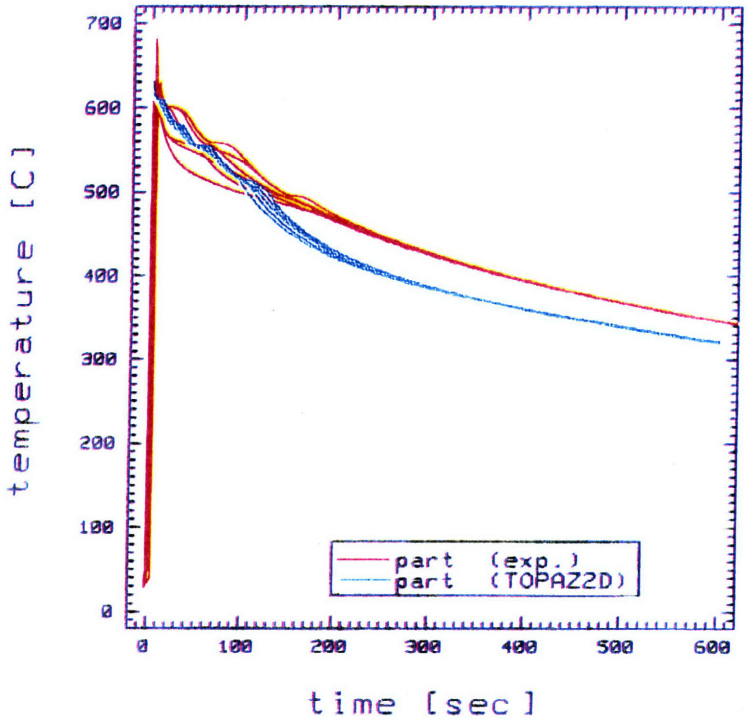

a)

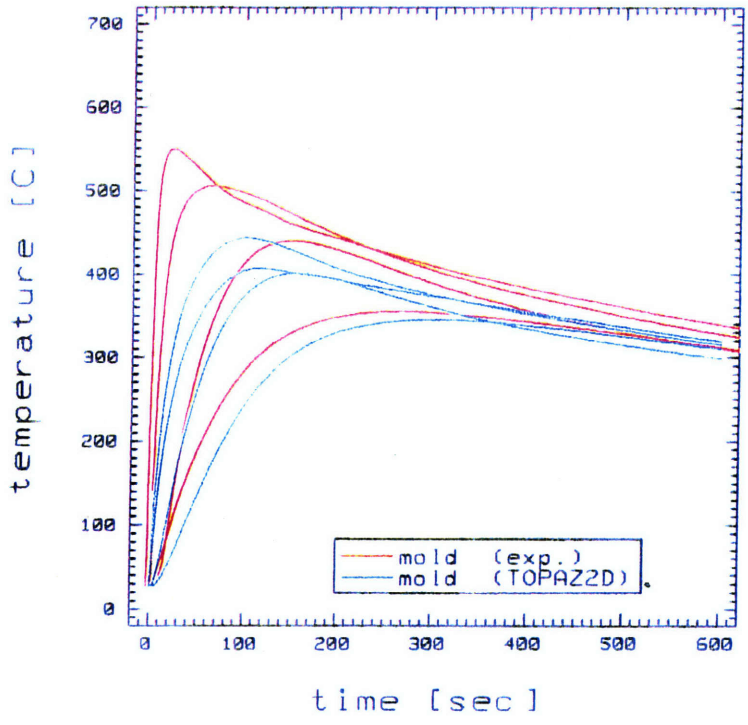

b)

FIGURE 16. Temperature history plots from thermal only analysis for: a) the casting; b) the mold.

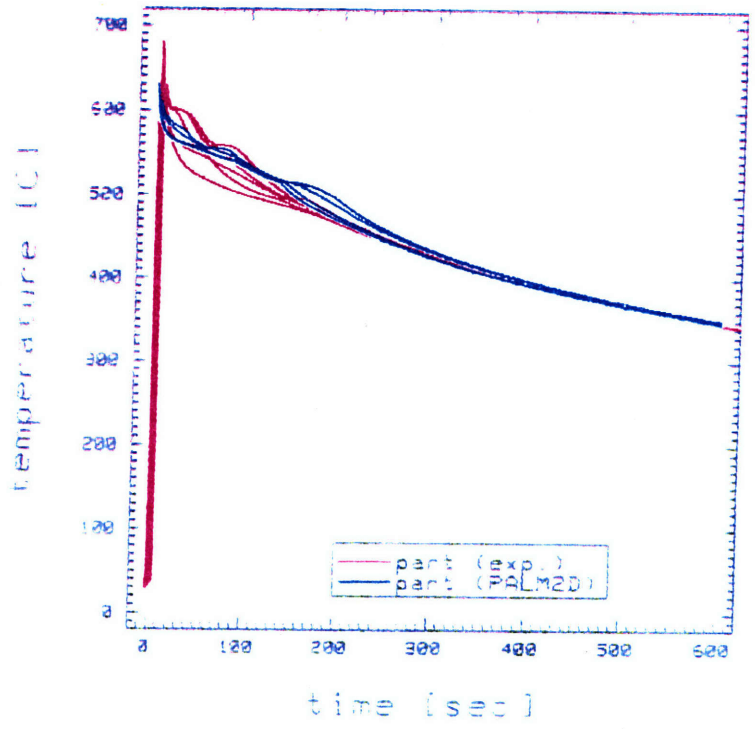

a)

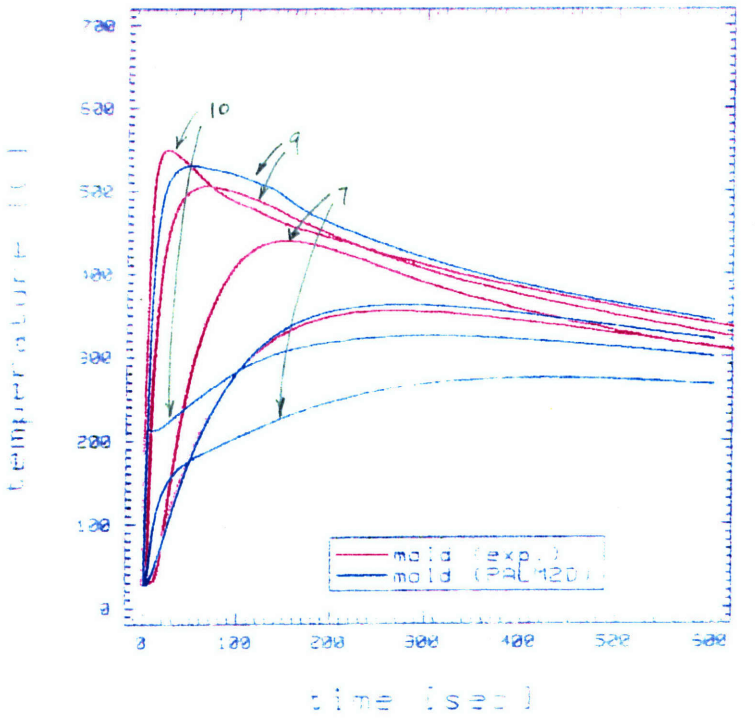

b)

FIGURE 17. Temperature history plot from thermomechanical analyses with rate independent flow strength model for: a) the casting and b) the steel cup.

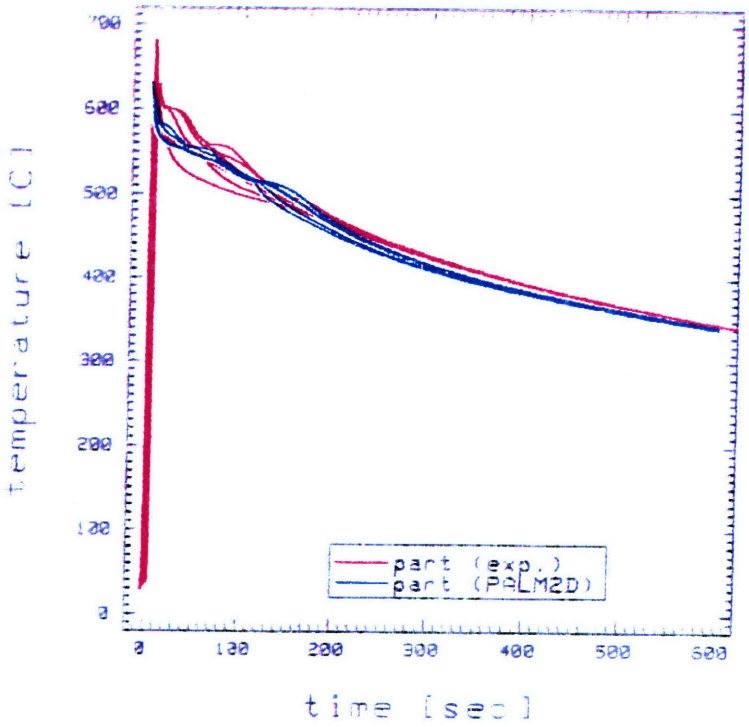

a)

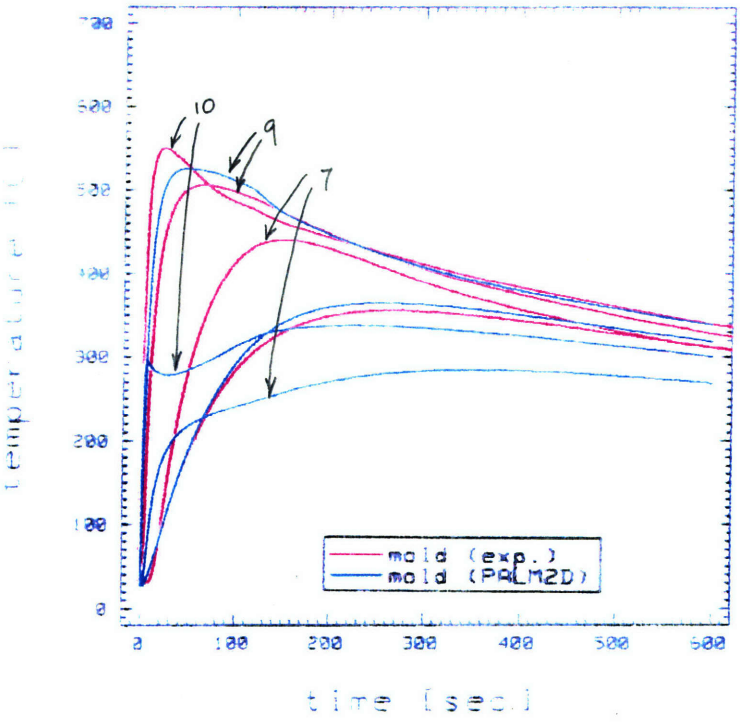

b)

FIGURE 18. Temperature history plot from thermomechanical analyses with rate dependent flow strength model for: a) the casting and b) the steel cup.

4.3.3 Mechanical Results

A comparison of the effective stress predicted by the thermomechanical analyses for the rate-dependent and rate-independent flow strength models is shown in Figure 17. The plot shows the accumulation of effective stress at the thermocouple positions as solidification progresses. The rate-independent model predicts stresses as high as 8.2x106 N/m^2 (about 450 psi!!) when it has cooled to about 600 ^oK. However, the rate-independent model generated predictions which are very very small, only about $75x10^{-3}$ N/m^2 (about $1x10^{-5}$ psi) at the same temperature. A plot showing in greater detail the stress prediction by the rate-dependent model is shown in Figure 18. Both models generate predictions with the same characteristics. The effective stress within the metal is virtually zero while it is still liquid. It begins to experience stress only after having cooled to the solidus temperature. The rate-independent strength model, however, predicted stresses which are many orders of magnitude higher. While the stresses were not measured in the experiment, the rate-dependent predictions are more plausible. It is physically unrealistic for the solidified casting to maintain such high level of residual stress. This error was caused by the large values of yield stress used in the rate independent model which was necessary for convergence in the analyses.

A plot of the prediction of effective strain rate is shown in Figure 20. The plot shows results from an analysis for Al 319 with the rate-dependent model. At the beginning of solidification, the strain rate is about $12.5x10^{-3}$ per second. As the part cools, the strain rate decreases to about $5x10^{-7}$ per second at 600 ^oK. This confirms our earlier assumption that ε will be very small at lower temperatures. Thus, the inaccuracy in our flow strength model at high strain rates during low temperature is not a matter of concern.

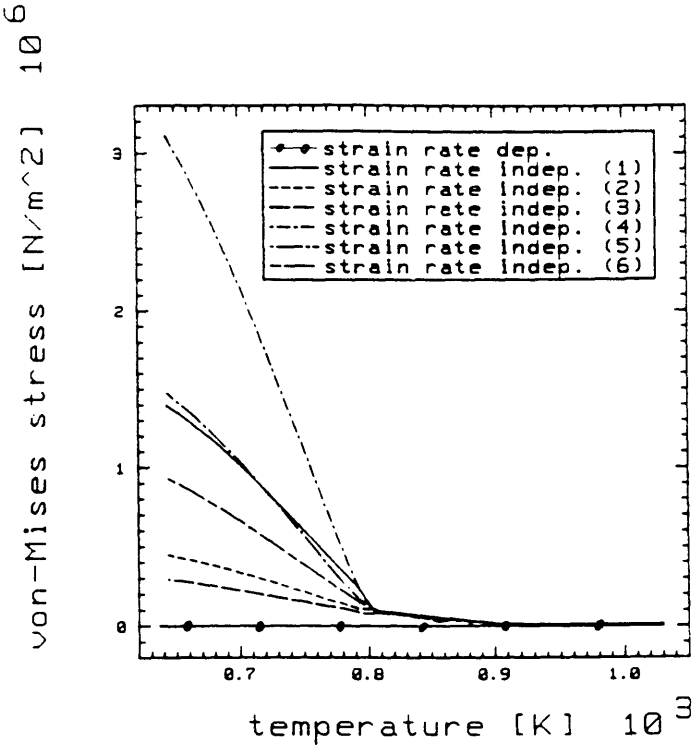

a)

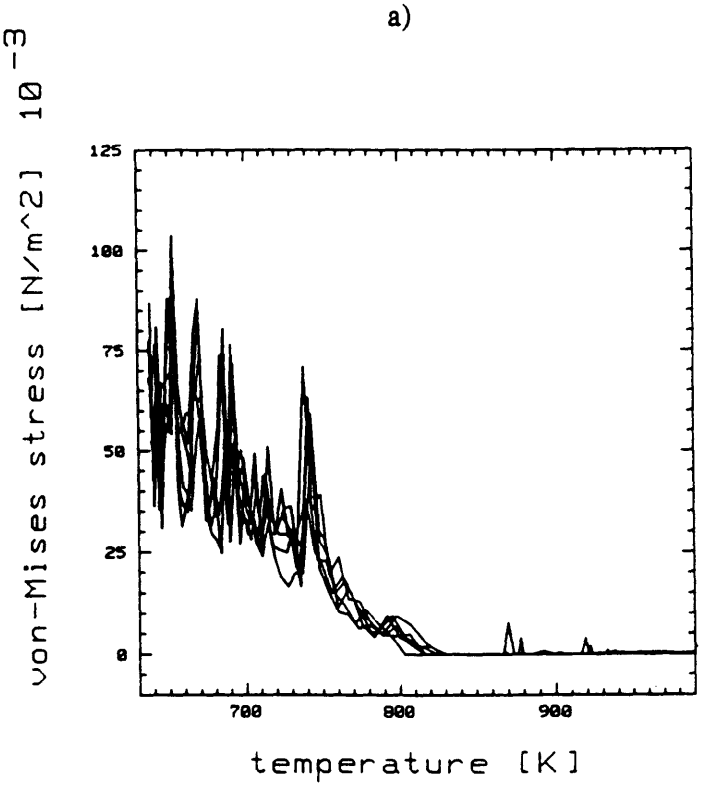

FIGURE 19. a) Effective stress within the pure aluminum casting as solidification progresses; b) detailed plot of effective stress for rate dependent model.

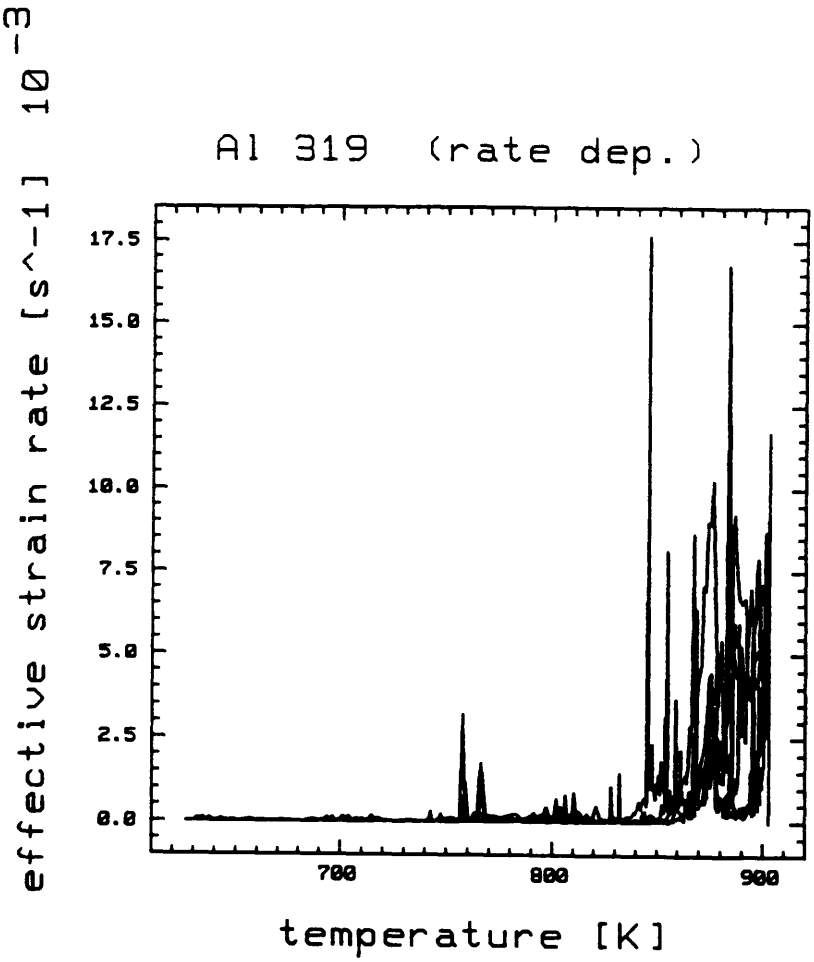

FIGURE 20. Effective strain rate within Al 319 casting as solidification progressed.

A comparison of the final shape prediction generated by thermomechanical analyses and the shape of the actual casting is shown in Figure 21. The analysis predicted a slighter cratering on the top surface and a side gap which is larger than that observed in the experimental casting. On the bottom interface, the analysis predicted only a very small gap. Graphical comparisons of the gap sizes are not provided in this work because they are not indicative of the success of the analysis. Both the experimental procedure and the analysis are very sensitive to the process parameters, and can generate results which are very different from trial to trial.

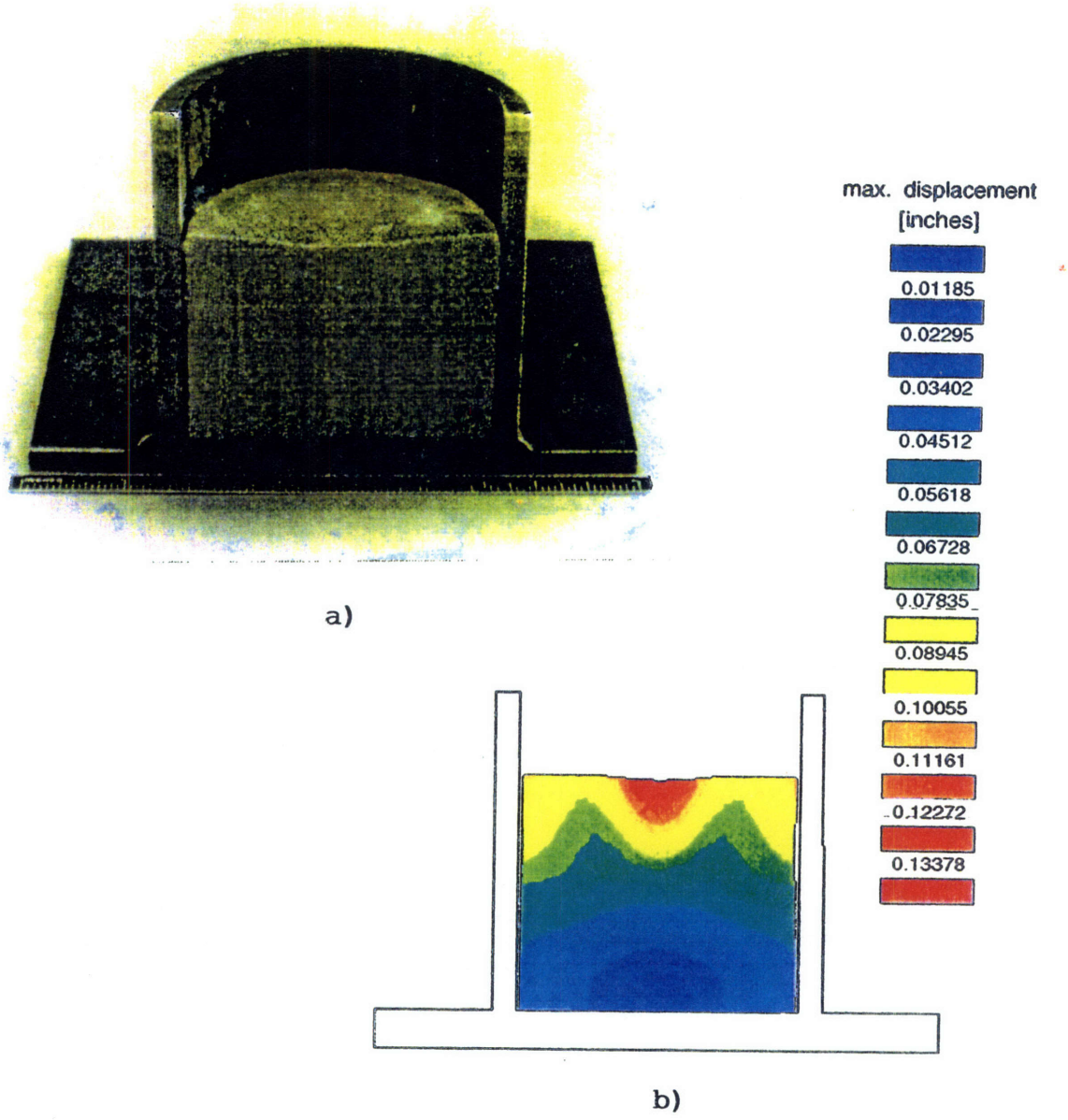

FIGURE 21. Comparison of a) the solidified casting and b) the finite element final shape prediction.

4.4 Conclusion

The simplicity of the cup casting experiment allows parameter studies to be performed efficiently. In our study, the interface gaps were confirmed to significantly reduce the cooling rate of the assembly. Thermomechanical analyses were then performed to address the deforming geometry. To model the strength of a metal near the melting temperature, a constitutive material model was created in which the strain rate dependency of a metal's flow strength was addressed. This model has been found to generate more realistic predictions of the residual stress upon solidification than the traditional strain rate independent model. The approach of using gap convection to model the transfer of heat across inter face gaps was also successful in modeling the decrease in cooling rate caused by the opening. Discrepancies in experimental and analytical results were difficult to reconcile because of the great number of process parameters involved.

The benchmarking of the experimental and finite element results is difficult. The thermocouples and LVDTs used during the experiment had introduced too many disturbance to the solidification process. The thermocouples conduct heat from the melt, thereby recording cooling rates which can be significantly higher than those in other regions of the casting. Also, the LVDTs inhibit the casting from shrinking freely as it cools. Thus, the experiment had introduced some uncertainty into the data.

Further finite element studies and better controlled experiments are necessary to perfect the casting model. It is unknown at this time why the finite element model did not predict the deformations upon solidification more precisely. For future studies, fine tuning the high temperature material properties and improving the imposed thermal conditions are recommended.

5.0 FINITE ELEMENT ANALYSIS OF HOT TEAR EXPERIMENT

After gaining experience in modeling casting problems, analyses for hot tear studies were performed. Previously, finite element analyses were performed for an experiment designed for benchmarking the hot tear susceptibilities of different alloys. Thermal and fluid analyses have been completed for a hot tearing test of aluminum sand castings. Mechanical analyses were deemed necessary before any predictions of hot tears can be made.

Attempts to perform loosely coupled thermal and mechanical analyses for the hot tear experiment were unsuccessful. The mesh for the model was very large and inefficient to debug. Finally, a much simpler casting assembly with the same characteristics as the hot tear experiment was designed so that results can be obtained more efficiently.

5.1 Background on Hot Tears

In sand casting processes of metal alloys, the presence of hot tears is one of many common causes of defects. Hot tearing can occur as a metal part solidifies in the sand mold. A casting develops tears if the stresses it experiences due to solidification and cool down shrinkage are greater than the ability of the metal to withstand them. The cause of hot tears is a complex matter. Factors such as solidification conditions, material properties, and part geometry all affect a casting's hot tear susceptibility. Typically, alloys are more prone to hot tears than pure metals because alloys solidify over a range of temperatures rather than at a discrete temperature. Hot tears take place in an alloy casting while it is still in the mushy zone, where both liquid and solid states coexist.

Hot tears result from stress concentrations within a casting caused by factors such as hindered contractions, hot spots, or extreme temperature gradients. The geometrical configuration of a casting can also have significant effects on its hot tearing tendency. Inadequate fillets in sharp corners can set up high stresses during solidification. Abrupt variations in the casting's thickness cause large variations in cooling rate, resulting in hot spots. In addition, sections which are I-shaped or U-shaped also experience high stresses during cooling due to restriction from the mold. In addition to the factors mentioned above, there are still many other issues which influence hot tearing susceptibility. Metallurgical casting parameters such as g ain size, alloy composition, molding sand compressibility, and gas content of the melt all have significant effects.

Engineers and scientists at General Motors Research Laboratories, Oak Ridge National Laboratory, Sandia National Laboratories, and LLNL have undertaken a study on hot tears in order to develop an aluminum alloy with high resistance to hot tearing. The project entailed designing and executing an experiment to be used for benchmarking of existing and any newly developed alloys. LLNL's role in the project was to provide the metallurgists and material scientists with insights to the casting procedure gained by performing finite element analyses of the experiment.

5.2 Analysis of Hot Tear Experiment

The experiment used was modeled after that developed by E.J. Gamber. [Gamber, 1959] Designed to show that cracks are more probable at sharp internal angles, the experiment entailed casting parts of various fillet radii. The specification for the specimens is shown in Figure 22. The effects of using end chills were also studied. Previously,

a finite element model of the experiment was created. [Leung, 1994] Thermal and fluid analyses were also performed. Results from these analyses suggested that castings with smaller filet radii were more susceptible to hot tears because of increased stress concentrations at the fillet and not due to any thermo-fluid conditions. Also, it was discovered that even with application of chills, the original casting design did not induce any hot tears. Thus, mechanical analyses of a redesigned hot tear specimen became necessary.

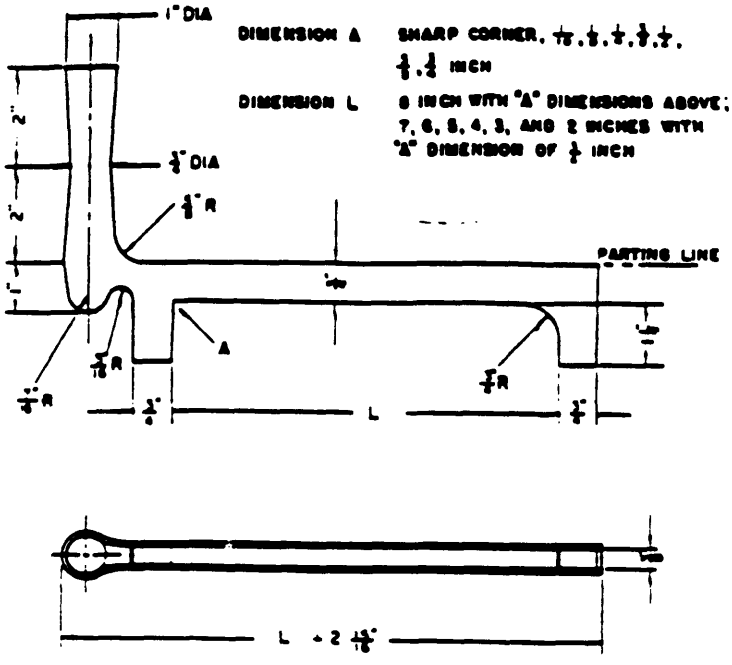

FIGURE 22. Part specification for hot cracking test.

5.2.1 Finite Element Model

To understand how geometric factors affect a casting's contraction upon cooling, mechanical analyses are being performed so that stress concentration within the casting can be observed. Also, the hot tear specimen has been redesigned by engineers at Oak Ridge National Laboratory to increase the likelihood of hot tearing. Finite element analyses for a casting with the internal fillet radius of 0.5 inches were attempted. The three-dimensional finite element mesh for the redesigned casting, mold, and chill is shown in Figure 23. The mesh contained 14810 nodes and 11010 elements.

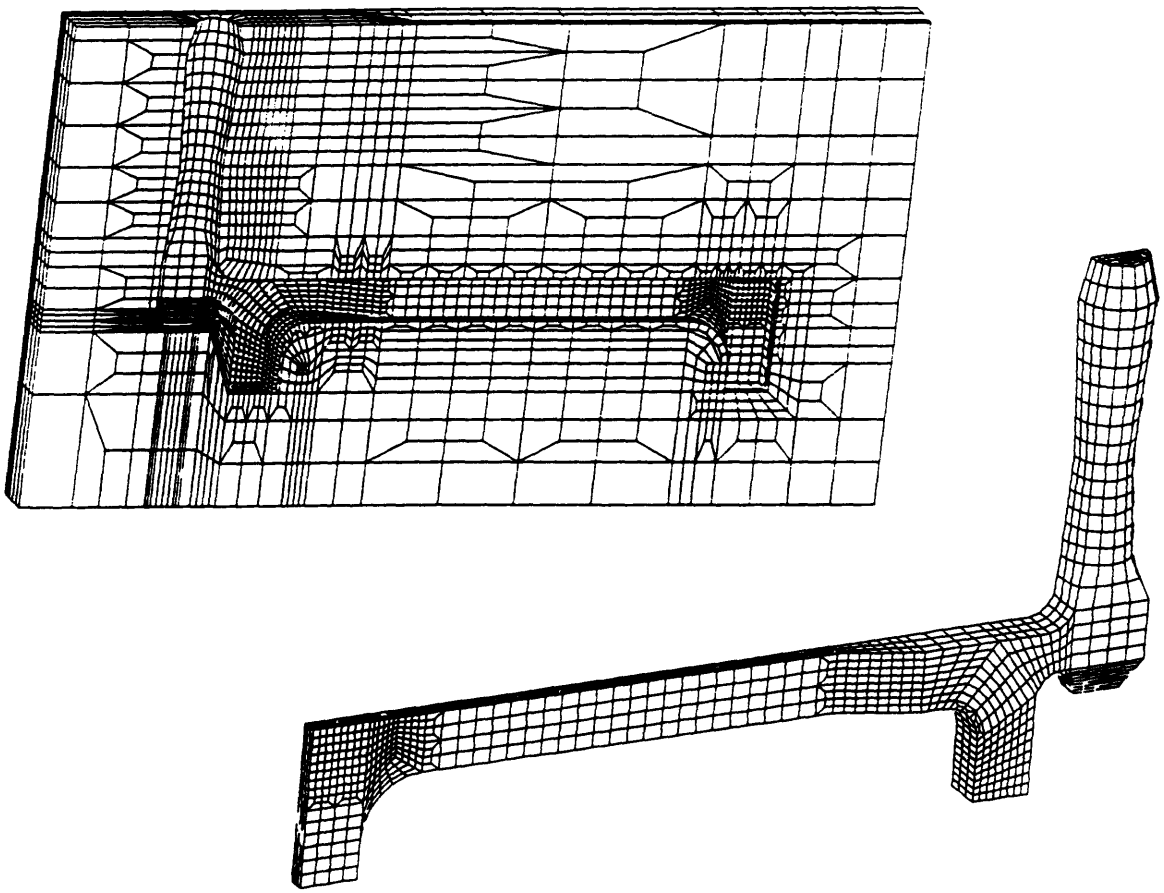

FIGURE 23. Three-dimensional finite element mesh for redesigned casting.

After creating the finite element mesh, thermal and mechanical analyses can be performed. A loosely coupled thermomechanical approach is taken because the features of PALM2D have not yet been implemented for three dimensional analyses. In a loosely coupled thermomechanical approach, thermal analysis is first performed. The temperature results are then used as inputs to a mechanical analysis.

5.2.2 Thermal Solution

Thermal only analyses were performed for a system which has already been filled. The Aluminum 319 was initially at 715 °C. The sand mold and copper end chill were initially at 25 °C. Analyses were performed in ProCAST[10] with the heat transfer coefficient at the casting-chill interface estimated as 2000 W/m^2 °K. The heat transfer coefficient at the chill-sand interface was estimated to be 200 w/m^2 °K. Fluid analyses were not performed since it was confirmed in the previous study that fluid effects during the filling process do not affect the accuracy of the thermal results.

The temperature versus time data were predicted at five different positions in the casting. There are four points distributed along a center line in the body, and one point in the center of the variable radius. Figure 23 shows the six nodal positions. The cooling curves generated from the ProCAST analyses are shown in Figure 24.

10.ProCAST is a finite element analysis package for casting systems. ProCAST is a trademark of UES, Inc., Dayton, Ohio.

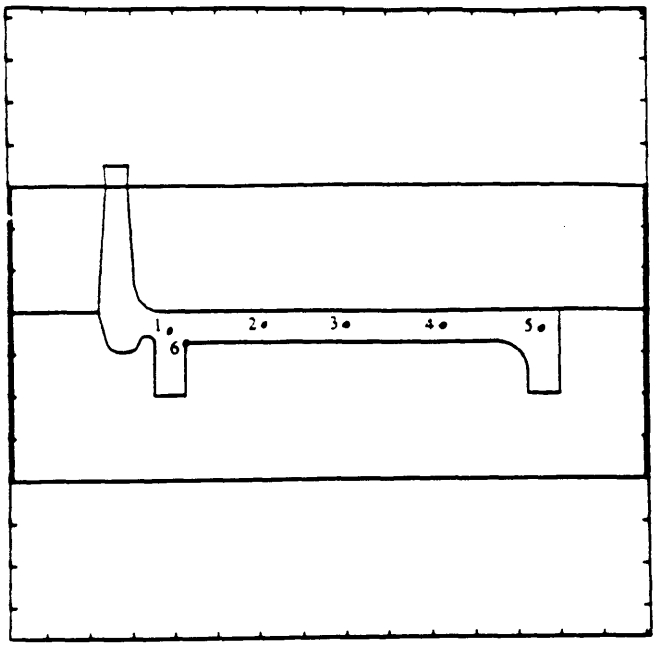

FIGURE 24. Six nodal positions selected for temperature history data.

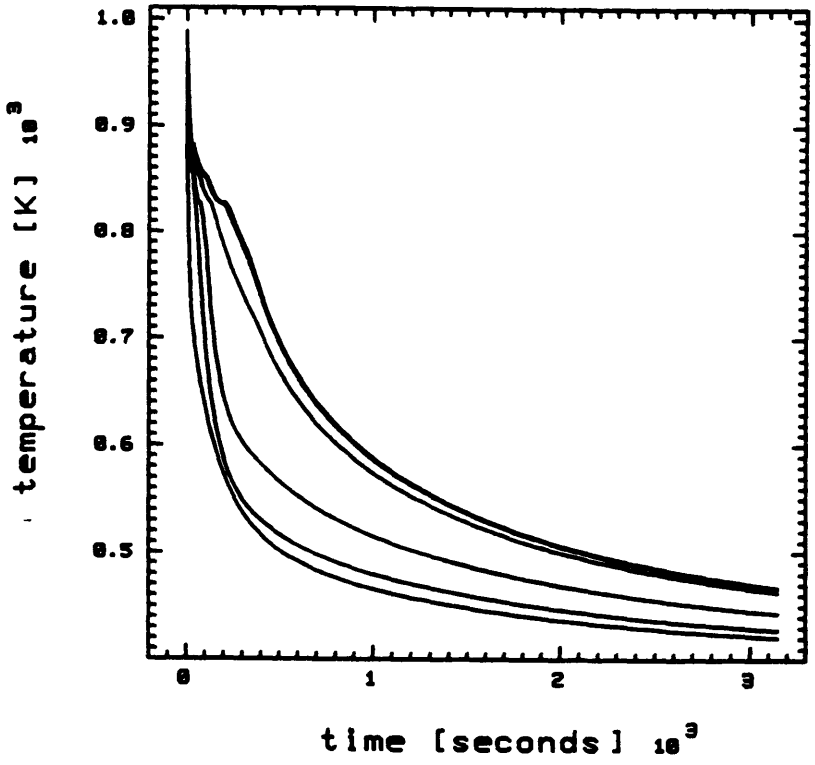

FIGURE 25. Set of cooling curves at various positions along the span of the casting.

5.2.3 Mechanical Analyses

Mechanical analyses are performed using NIKE3D. The temperature results from ProCAST were processed by ProCONVERT[11] into a form compatible as temperature time-state data for NIKE3D. A simple elastic-plastic material model is used (Shown in Appendix D.) The properties for silica sand were estimated from results of triaxial compression tests for dense fine silica sand. [Duncan et. al., 1970] In addition, a mechanical slideline is applied at all of the material interfaces to allow the casting to deform independently of the casting and mold.

5.2.4 Results

Unfortunately, the mesh for the hot tear experiment is too large, making the finite element analyses very costly and time ineffective. Many difficulties were encountered in achieving convergence of solution in the initial time steps. This was due to the lack of experience in performing such analyses and the inefficiencies of a large mesh. Debugging was almost impossible since the model required a typical turn-around time of about 24 hours on the Cray Computers as the series of iterations and reformations are performed to attempt convergence.

As a result, analyses of the hot tear experiment were suspended. Instead, a much simpler model was created which has all the characteristics of the hot tear experiment. This smaller mesh allowed us to gain insight to the hot tear experiment in a much more effective manner.

11.ProCONVERT is a program used at LLNL to make ProCAST temperature ouputs compatible as NIKE3D input.

5.3 Simplified Hot Tear Casting

A simplified hot tear casting assembly was designed to emulate the original hot tear experiment. The specification for the newly designed casting is shown in Figure 26. All of the characteristics of the original experiment had been incorporated into the simplified design. The new design is also for the casting of Al 319 in silica sand. The casting has a U-shape to provide constraints to thermal contractions. Also, a wide front section is connected to a very thin end section by a transition region. In addition, the span of the casting was designed to be slender and long so that a greater temperature gradient can be achieved across it.

5.3.1 Finite Element Model

The finite element mesh for the newly designed casting and mold is shown in Figure 27. The mesh contains 1304 nodes and 768 elements. (The size of the mesh has been reduced by a factor of more than ten!!) Identical thermal and mechanical conditions were assigned, and thermal analyses were again performed by ProCAST. Subsequently, NIKE3D analyses were performed. Convergence of the solution was still very difficult to achieve.

Currently, analyses were successful only when the number of time steps between equilibrium iteration was set to two. Ideally, iterations should be performed at every time step. Thus, the accuracy of the finite element prediction is likely to be compromised. Also, the number of elements in the mesh had been kept to a minimum to decrease the computer run time. This small mesh takes only about 340 seconds on a Cray Computer. While better results can be obtained with a finer mesh, the current results still provided much insight to the original casting experiment.

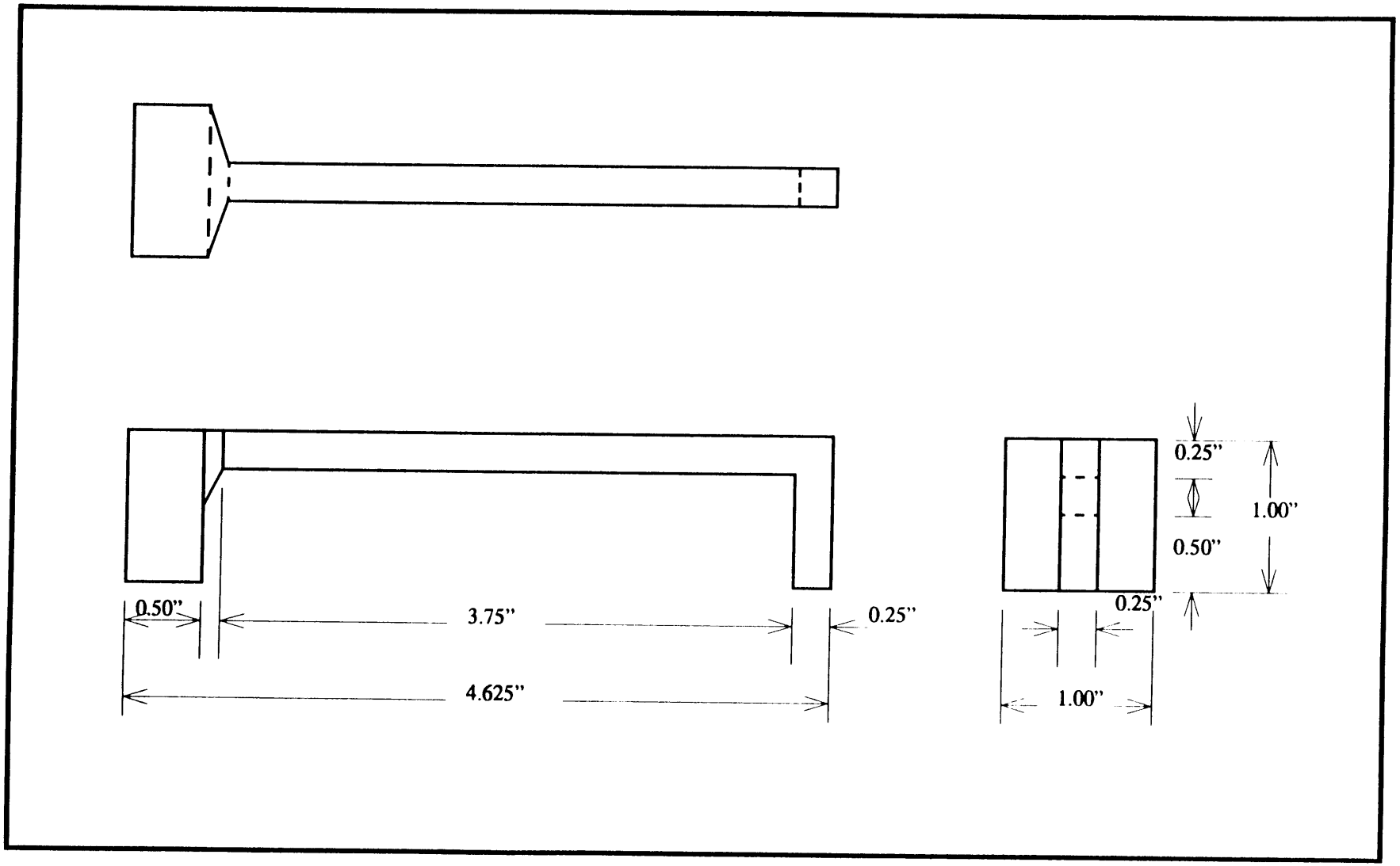

FIGURE 26. Specification for simplified hot tear casting and mold.

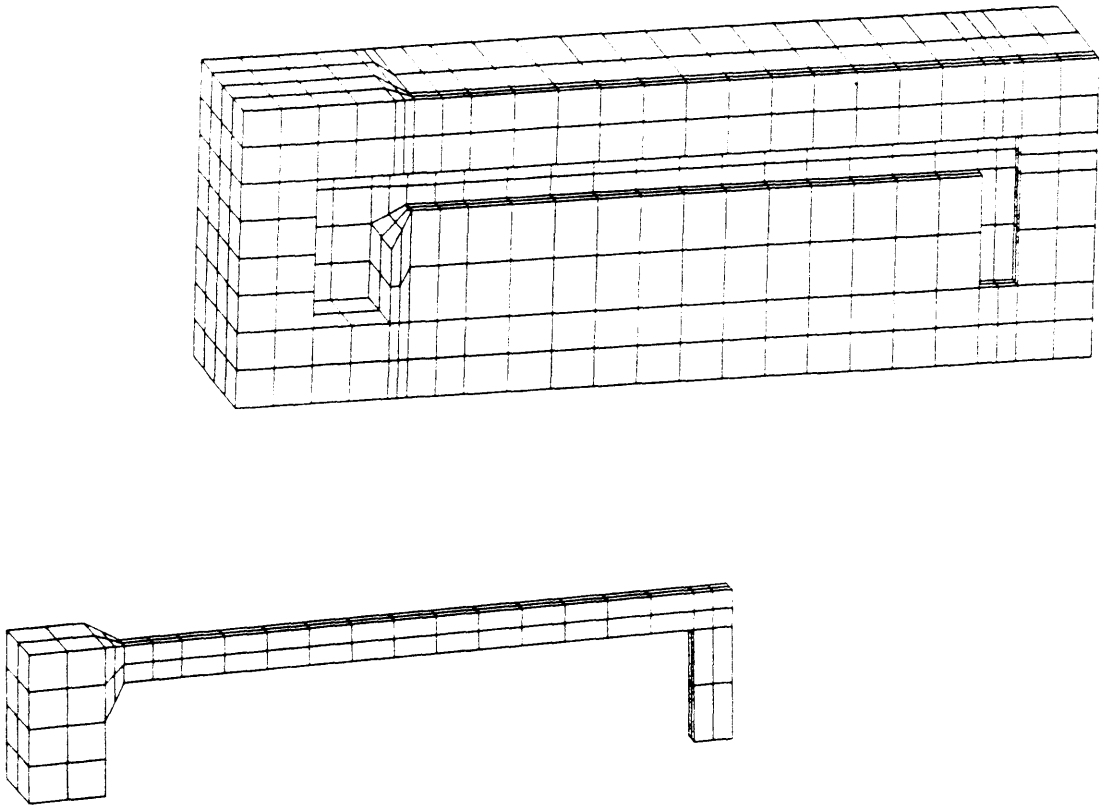

FIGURE 27. Finite element mesh for simplified hot tear casting and mold.

5.3.2 Results

Temperature fringe plots are shown in Figure 28. The first plot shows the casting at 8 seconds and the second at 50 seconds. A large temperature gradient can be observed across the casting because of its thin cross section and long length. The thinner end is consistently the coolest part of the casting. The gradients progresses toward the thicker end, with the big end column staying considerably hotter than the rest of the casting.

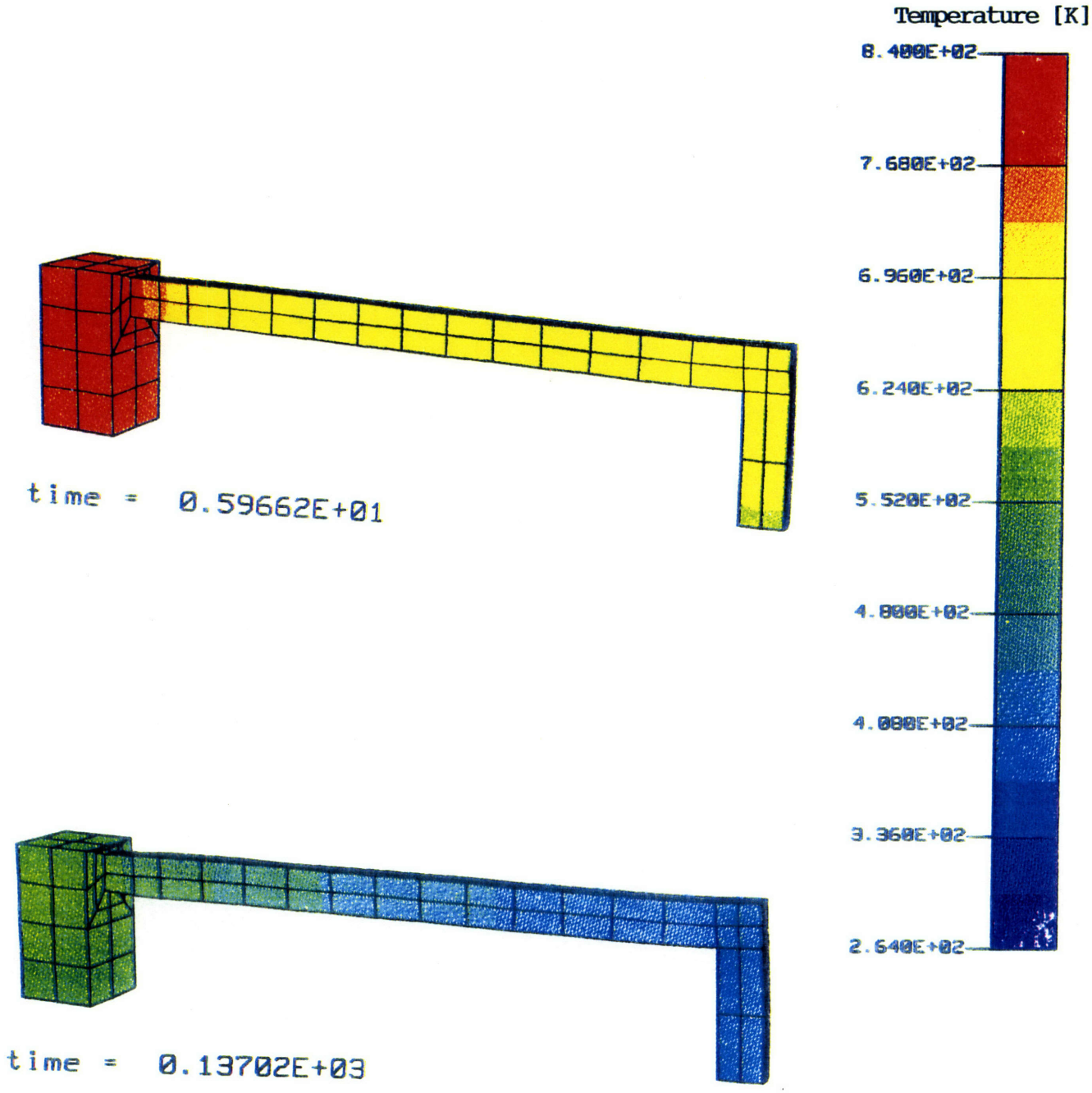

FIGURE 28. Temperature fringe plot.

As the casting solidifies from its initial temperature of 715 °C in the sand mold at 25 °C, it experiences contractions and begins to deform. Figure 29 shows a finite element prediction of the shapes of the casting and mold at the end of 300 seconds. The contraction of the casting is constrained by the two legs at the front and back. Thus, as the casting contracts, the span experiences a bending motion. The two ends are then lifted upward, deforming the sand mold in the process.

A fringe plot of the effective stress within the casting is shown in Figure 30. It can be observed that the span of the casting generally experiences higher stresses than do the two end regions. More importantly, the region with the highest stress occurs in the area where the most severe amount of bending is experienced.

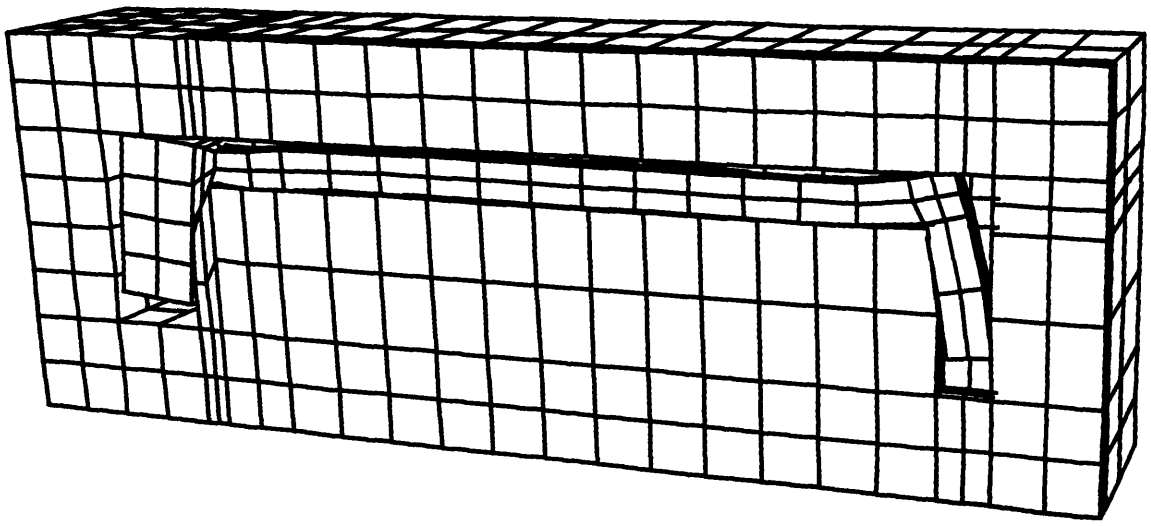

FIGURE 29. Deformation of casting and sand mold after 300 seconds. (Displacement magnified by a factor of 3 for clarity.)

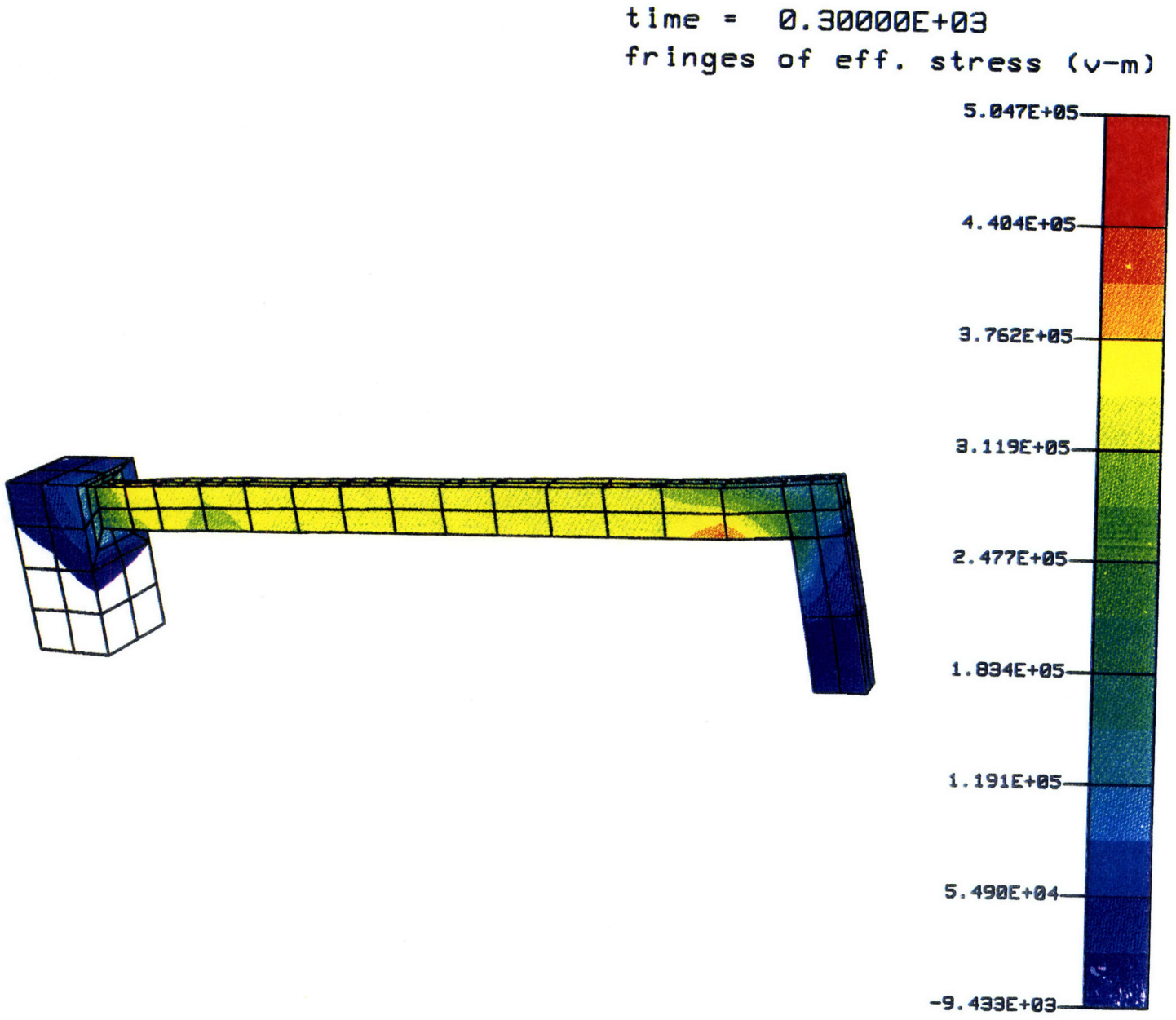

FIGURE 30. Fringe plot of effective stress in casting after 300 seconds shows maximum stress in the region where bending is most severe.

5.4 Discussion

Although the analysis of the simplified casting design yielded only approximate predictions, it provided much insight into why the original hot tear experiment was unsuccessful. Previously, the hot tear specimen was thought to have failed because of the lack of temperature gradients in the span. Thus, the front leg was widened so that the cooling rate can be decreased. This design change was made with the intention that the metal in the widened leg will remain mushy longer and become subjected to contraction forces as the thinner span and back leg contracted. However, for this design to induce hot tears at the variable radius, the span must be long and slender enough so that a very significant temperature gradient is present across the casting. The redesigned casting, however, did not have a span slender enough and was likely to be unsuccessful again in producing hot tears in the specimens. In fact, the only effects of the widened front leg is that the stress it experiences will be reduced because of the increase in cross sectional area. Therefore, the region near the variable radius has actually been made less sensitive to hot tears.

In order for hot tears to occur in a specimen, the part must have regions of abrupt variation in cross section and extreme temperature gradients. In addition, the geometry of the casting and mold must provide enough geometric constraint that any thermal contractions in the part is hindered. Results from the finite element analyses have shown that this condition is met neither in the original nor the simplified hot tear design. Because the two end legs, especially the thinner back leg, are not massive enough, they do not sufficiently prohibit the contraction of the span. As a result, the span is allowed to contract by bending and lifting the two ends. Thus, the ends must be made massive

enough so that this bending action is minimized to provide maximum hindrance to the contraction of the span.

5.5 Conclusion and Recommendations

Finite element analysis of the original hot tear experiment was unsuccessful because of its large mesh size. Because of the lack of experience in performing thermo-mechanical analyses, much debugging was required. The debugging process was very time consuming and inefficient because the model was so cpu intensive. Therefore, a simplified hot tear model with the characteristics of the original one was created. The thermal and mechanical analyses provided insight to the flaws in the design of the hot tear specimen. The geometry of the part did not induce a large enough temperature gradient across the casting. In addition, the shape of the casting provided insufficient hindrance to thermal contraction in the span.

In designing a new hot tear specimen, simplicity in the geometry is important if finite element analysis predictions are desired. As new features are being implemented into the thermomechanical approach, much debugging and parametric studies are necessary. Large models will be too time and cost inefficient for this purpose.

6.0 Conclusion

While the ultimate goal of this project was to perform thermomechanical analyses for a hot tear experiment, development of the finite element model required benchmarking analyses to be first performed for a much simpler casting procedure. Insight into the solidification process was then applied to the hot tear analyses.

Finite element analyses of casting processes performed using the coupled thermal and mechanical approach are capable of taking into consideration the changes in geometry often present during solidification. An approach to model the transfer of heat across interface gaps was presented. The interface gaps and surface deformations prediction showed some disagreement with experimental results. The discrepancies can be attributed to simplifications made in the finite element model which were necessary to keep the model robust. Difficulties in controlling the experiment also introduced uncertainty into the experimental data. More importantly, the solidification process is highly sensitive; and repeated casting trials often do not generate identical results even under the same apparent conditions. Thus, it can be concluded that our model is satisfactory in providing an approximation to the gaps and surface deformations formed during solidification.

An approach to model the flow strength of metals at melting range temperatures was also developed using rate dependent plasticity. This model was found to generate more realistic results than previous analyses using a creep rate independent model, which had erroneously predicted high residual stresses within the casting even after complete solidification.

Finite element analyses of the hot tear experiment were found to be inefficient because of the large mesh size. A simplified hot tear design with the characteristics of the original one was created so that analyses could be performed more efficiently. Preliminary thermal and mechanical analyses predicted flaws in the hot tear design. The geometry of the casting was found to provide insufficient hindrance to thermal contraction in the span.

Because of time limitations, analyses using the models for interface gaps and rate-dependent plasticity flow strength were not performed. For future studies, it is recommended that the hot tear design be revised before any further analyses is performed. While more detailed finite element meshes can generate more accurate predictions, simpler models are better suited for the purposes of debugging and parameter studies. With more experience in performing thermomechanical analyses, the interface gap and rate dependent flow strength models can be further improved.

Bibliography

1. "Heat Transfer Data Book", General Electric Company Corporate Research and Development, November 1970.

2. Campbell, John. Castings, Butterworth-Heinemann Ltd., Oxford. (1991)

4. Crandall, S., Dahl, N., and Lardner, T. An Introduction to the Mechanics of Solids. McGraw-Hill Book Company: New York, 1978.

5. Duncan, James M., and Chang, Chin-Yung, "Nonlinear Analysis of Stress and Strain in Soils", Journal of the Soil Mechanics and Foundation Division, Proceedings of the American Society of Civil Engineers, September 1970.

6. Frost, Harold J. and Ashby, Michael F., Deformation-Mechanism Maps: The Plasticity and Creep of Metals and Ceramics. Pergamon Press: Oxford, 1982, pp 26-27.

7. Gamber, E.J., "Hot Cracking Test for Light Metal Casting Alloys", Transactions American Founrymen Society, vol. 67, 1959. pp 237-241.

8. Harper, J. G., Shepard, L.A. and Dorn, J.E., "Creep of Aluminum Under Extremely Small Stresses", Acta Metallurgica, vol. 6, July 1958, pp 509-518.

9. Ho, K., and Pehlke, R. D., "Mechanisms of Heat Transfer at a Metal-Mold Interface", American Foundrymen Transactions, 1984, pp 587-598.

10. Jacobi, H. Arch. Eisenhuttenwesen, vol. 47, pp 441-446. (1976)

11. Kornblum, B., and Leung, W., "Comparison of ProCAST with NIKE3D for Concentric Cylinder Thermal Stress Test Problem", Lawrence Livermore national Laboratory, October 1994.

12. Leung, W., "Finite Element Analyses of Hot Tearing Test for Aluminum Sand Castings", S.B. Thesis for M.I.T., May 1994.

13. McClintock, Frank A. and Argon, Ali S., Mechanical Behavior of Materials. Redding, Massachusetts: Addisson-Wesley Publishing Company, 1966.

14. Raboin, Peter J., "A solidification Constitutive Model for NIKE2D and NIKE3D", Lawrence Livermore National Laboratory, January 1994.

Appendix A:

Properties of Pure Aluminum

Material	Temperature [K]	Thermal Conductivity [W/m-°K]	Specific Heat [KJ/Kg-°K]
Pure Aluminum	273	236	- -
	298	- -	0.903
	300	237	0.905
	400	240	0.950
	500	237	0.998
	600	232	1.043
	700	226	1.090
	800	220	1.135
	900	213	1.181
	933.2 (s)	211	- -
	933.2 (l)	90.7	1.086
	1000	93	1.086
	1100	96.4	1.086
	1200	99.4	1.086
	1300	102	1.086
	1400	105	1.086
	1500	107	1.086

Table A1. Thermal Properties of Pure Aluminum.[12]

Density: $\rho_s = 2702$ Kg/m3

Heat of Fusion: $\Delta h_f = 397.5$ KJ/Kg

12.Pehlke, R.D., Jeyarajan,A., and Wada, H.. "Summary of Thermal Properties for Casting Alloys and Mold Materials", University of Michigan, December 1982.

Temperature [K]	Young's Modulus [N/m^2]	Poisson's Ratio	Secant CTE[a] [1/K]
298	69.00E+09	0.33	23.90E-06
598	69.00E+09	0.33	23.90E-06
900	50.00E+09	0.33	32.19E-06
933	10.00E+09	0.33	67.43E-06
1500	1.00E+09	0.33	15.37E-06

a. CTE stands for Coefficient of Thermal Expansion

Table A2: Mechanical Properties of Pure Aluminum.

Temperature [K]	Flow Strength [N/m^2]
298	90.00E+06
598	45.00E+06
900	1.00E+04
933	1.00E+04
1500	1.00E+04

Table A3: Rate Independent Flow Strength for Pure Aluminum.

Temperature [K]	Flow Strength Coeff., A[a]	Strain Rate Sensivity, m
187	1.000E-02	1.020E-02
280	1.018E+01	7.143E-02
373	4.130E+01	1.111E-01
420	9.581E+01	1.270E-01
467	2.144E+02	1.429E-01
515	2.698E+02	1.761E-01
560	1.542E+03	1.818E-01
653	9.584E+03	2.273E-01
746	3.440E+04	2.500E-01
797	1.477E+04	3.333E-01
1000	1.298E+00	1.000E+00
1500	1.298E+00	1.000E+00

a. Values for A were determined from the equation $\sigma=1.435e8(S)(\varepsilon/A)^m$, where S has a constant value of 1. The scaling factor of 1.435e8 was a large value arbitrarily chosen so that A will not have a value too small for computer calculations. Strain rate has unit of 1/s; and flow strength has unit of N/m^2.

Table A4: Rate Dependent Elasto-Plasticity Data for Flow Strength Model.

Appendix B:

Properties of Aluminum Alloy 319

Material	Temperature [K]	Thermal Conductivity [W/m-°K]	Specific Heat][a] [KJ/Kg-°K]
Aluminum Alloy 319	29.8	109.0	
	273.1		0.8996
	373.0		0.963
	765.0		1.086
	788.0	95.48	
	878.0	93.00	
	890.0	93.00	1.070
	1500.0	107.0	1.070

a. Heat of Fusion, $\Delta h_f = 389.0$ KJ/Kg, is not included in the data given here.

Table B1: Thermal Properties of Aluminum Alloy 319.

Temperature [K]	Fraction Solid
765	1.0
771	0.995
778	0.98
789	0.94
826	0.77
827	0.60
848	0.47
856	0.31
880	0.11
882	0.0

Table B2: Data Points for Fraction Solid Curve.

Temperature [K]	Density [kg/m^3]
0	2795
788	2560
878	2380
1173	2315

Table B3: Density Data

Temperature [K]	Young's Modulus [N/m^2]	Poisson's Ratio	Secant CTE[a] [1/K]
298	69.00E+09	0.33	23.90E-06
598	69.00E+09	0.33	23.90E-06
730	50.00E+09	0.33	
760	10.00E+09	0.33	
788			57.69E-06
877	1.00E+09	0.33	90.97E-06
1173			72.02E-06
1500	1.00E+09	0.33	

a. CTE stands for Coefficient of Thermal Expansion

Table B4: Mechanical Properties of Aluminum Alloy 319.

Temperature [K]	Flow Strength [N/m^2]
298	90.00E+06
598	45.00E+06
730	1.00E+04
790	1.00E+04
877	1.00E+04
1500	1.00E+04

Table B5: Rate Independent Flow Strength for Al 319.

Temperature [K]	Flow Strength Coeff., A[a]	Strain Rate Sensivity, m
373	2.778E-08	8.774E-03
422	4.986E-07	6.893E-02
477	3.139E-06	1.303E-01
500	1.317E-05	1.487E-01
525	2.148E-04	1.594E-01
540	4.026E-04	1.701E-01
565	3.968E-03	1.786E-01
595	2.147E-01	1.915E-01
620	3.489E+00	2.000E-01
630	1.167E+01	2.083E-01
638	1.013E+01	2.165E-01
653	3.566E+01	2.273E-01
700	1.420E+03	2.400E-01
746	7.609E+04	2.500E-01
797	2.679E+04	3.333E-01
1000	1.582E+00	1.000E+00
1500	1.582E+00	1.000E+00

a. Values for A were determined from the equation $\sigma=1.75e8(S)(\varepsilon/A)^m$, where S has a constant value of 1. The scaling factor of 1.75e8 was a large value arbitrarily chosen so that A will not have a value too small for computer calculations. Strain rate has unit of 1/s; and flow strength has unit of N/m^2.

Table B6: Rate Dependent Elasto-Plasticity Data for Flow Strength Model.

Appendix C:

Properties of Carbon Steel

temperature [K]	Specific Heat [J/Kg °K]	Thermal Conductivity [W/m^2 °K]
200	434	60.5
400	487	56.7
600	559	48.0
800	685	39.2
1000	1169	30.0
1500	1169	30.0

Table C1: Thermal Properties of Carbon Steel

temperature [K]	Young's Modulus [N/m2]	Poisson's Ratio	Secant CTE [1/K]	Yield Stress [N/m2]
200	2.00E+11	0.3	10.0E-06	7.0E+08
1500	2.00E+11	0.3	10.0E-06	7.0E+08

Table C2: Mechanical Properties of Carbon Steel

(Density = 7800 Kg/m^3)

Appendix D:

Properties of Silica Sand and Al 319 used in Hot Tear Analysis

Temperature [K]	Young's Modulus [N/m^2]	Poisson's Ratio	Secant CTE	Yield Strength [N/m^2]
298	10.000E+06	0.33	2.390E-05	9.000E+07
598	7.100E+06	0.33	2.390E-05	4.500E+07
790	1.400E+06	0.33	5.770E-05	1.000E+05
877	1.400E+06	0.33	9.100E-05	5.000E+04
1500	1.400E+06	0.33	7.200E-05	5.000E+04

Table D1: Mechanical Properties of Aluminum 319.

Temperature [K]	Young's Modulus [N/m^2]	Poisson's Ratio	Secant CTE	Yield Strength [N/m^2]
298	6.300E+04	0.20	5.000E-06	1.000E+05
598	6.300E+04	0.20	5.000E-06	1.000E+05
790	6.300E+04	0.20	5.500E-06	1.000E+05
877	6.300E+04	0.20	6.000E-06	1.000E+05
1500	6.300E+04	0.20	6.000E-06	1.000E+05

Table D2: Mechanical Properties of Silica Sand.